University of Iceland
Faculty of Natural Sciences
Department of Physics

RH-08-99

Effects of shape on the far-infrared absorption of quantum dots

by

Ingibjörg Magnúsdóttir

A thesis submitted in partial satisfaction of the
requirements for the degree of
Master of Science in Physics at the University of Iceland

Committee in charge:
Viðar Guðmundsson, Chair
Ragnar Sigurðsson

Reykjavík
June 1999

Contents

Chapter 1

Introduction

Quantum dots are small electron systems, a few nanometers in diameter, which can be realized by means of modern fabrication techniques. The electrons' motion is confined in all three dimensions, leading to a discrete energy spectrum, in that sense, a quantum dot is in fact a zero dimensional structure. The discrete energy spectrum and the man-made confining potential characterize the quantum dot as an *artificial atom*. The typical energy level spacing of a quantum dot lies in the range of a few meV, i. e. within the far-infrared (FIR) range of the electromagnetic spectrum. The FIR absorption has been measured for quantum dots of various shapes. In the model calculations presented in this thesis, such quantum dots have been modelled with a general confinement potential, which is in fact a multipole expansion in two dimensions. When the circular symmetry is broken, the angular momentum is no longer conserved.

The thesis is divided into the following parts:

- Before focusing on the model calculations, the methods of fabricating quantum dot structures for FIR spectroscopy will be sketched (Chapter 2). In the experiments, a magnetic field is applied perpendicular to the plane the electrons move in, having important effects on their energy spectra and absorption. For circular or elliptic quantum dots, a harmonic confinement potential has proven to be a realistic approximation. For their FIR absorption, the generalized Kohn theorem applies. It states that FIR radiation couples only to the center-of-mass motion of the electrons. This will be formulated in Chapter 2.

- The properties of a single electron quantum dot will be discussed in Chapter 3, for circular parabolic, elliptic and square symmetric confinement potentials. Effects of the confinement on energy spectra, calculated as a function of the external magnetic field, will be shown. A solution method to Schrödinger's equation, for the general confinement potential, will be given.

- For more than one electron in a dot, their mutual Coulomb interaction has important effects. The typical Coulomb energy is of the order of 10 meV, which is

of the same order or larger than the confinement energy. The Coulomb interaction will be taken into account within the Hartree approximation (Chapter 4).

- When the energy levels and eigenstates, of the interacting electrons, have been calculated in the Hartree approximation, the FIR absorption of electron system can be calculated with the time-dependent Hartree approximation. Expressions for the dielectric tensor and the power absorption are derived in Chapter 5. Absorption spectra will be shown for harmonic quantum dots (Chapter 6) and square symmetric dots (Chapter 7). Results will be compared with the predictions of Kohn's theorem for harmonic dots, whereas traces of the Coulomb interaction will be identified in the absorption spectra of square symmetric dots.

Chapter 2

Quantum dots and far-infrared spectroscopy

In this chapter, the realization of a two dimensional electron gas (2DEG) on the interface between GaAs and $Al_xGa_{1-x}As$ semiconductors is described. Fabrication of arrays of quantum dots from the 2DEG, suitable for far-infrared spectroscopy, is discussed. For circular dots, a circular symmetric parabolic confinement potential has proven to be a realistic approximation. For such dots in a perpendicular magnetic field, the generalized Kohn theorem has important consequences. It states that FIR radiation only couples to the center-of-mass motion of each dot, due to its long wavelength ($> 1\mu$m) compared to the diameter of the dots (50-500 nm). A proof of the theorem, by P. A. Maksym and T. Chakraborty [1], is given. Generalized results, for a parabolic confinement with arbitrary strength in each dimension, are sketched [2].

2.1 Two dimensional electron systems

GaAs and $Al_xGa_{1-x}As$ are semiconductors with similar lattice constants (≈ 5.65 Å for GaAs) and can thus be brought together to form a heterostructure. They are grown on top of each other by Molecular Beam Epitaxy (MBE). Their different bandgaps, 1.5 eV for GaAs and $(1.5 + 0.7x)$ eV for $Al_xGa_{1-x}As$, lead to a band-discontinuity at their interface (Fig. 2.1). The coupling between the conduction and valence bands can be neglected in FIR experiments, due to their wide bandgaps.

At very low temperatures, semiconductors are insulating. However, if they are selectively doped, free carriers are introduced. By doping the $Al_xGa_{1-x}As$-layer with Si-donors (concentration of the order 10^{18} cm^{-3}), the conduction electrons move to the GaAs-layer, since it has a lower bandedge, and leave behind positively charged Si ions. A layer at the interface is left undoped, the so-called spacer layer. It separates the electrons from the Si-ions and thus reduces impurity scattering. This results in the (conduction) band structure in Fig. 2.2. A triangular potential is formed at the interface and the conduction electrons are confined by this potential to a layer

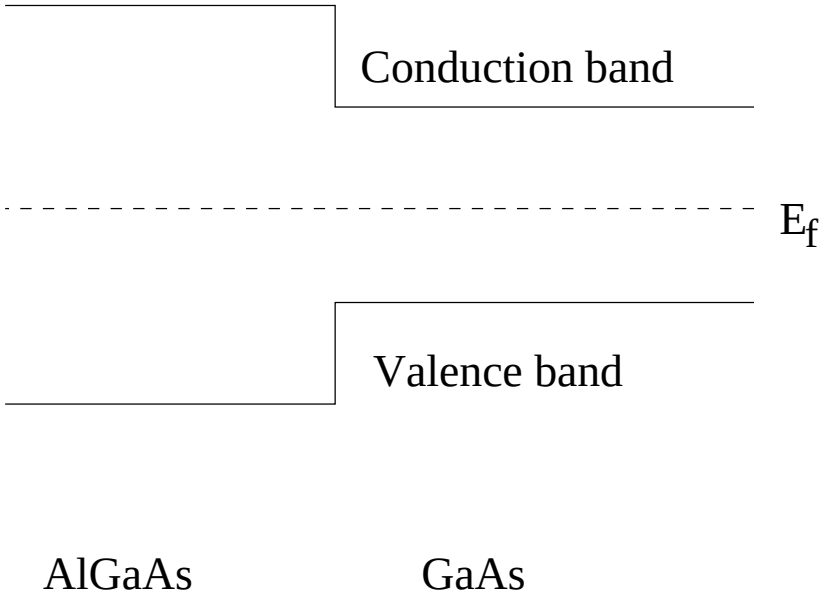

Figure 2.1: A schematic picture of the bandstructure at the heterostructure interface. The difference in bandgaps leads to a discontinuity at the interface. The GaAs has a lower conduction band edge than $Al_xGa_{1-x}As$.

of thickness $\approx$ 10 nm. This leads to a quantization of the electron motion in the growth direction of the structure and subbands are formed in the triangular well. If only the lowest subband is occupied, the electron motion in the growth direction is frozen out. The electrons are then confined to the two-dimensional interface [3]. The electron motion separates into a bounded motion perpendicular to the interface and an in-plane free motion. The energy levels take the form [4]

$$E = E_n + \frac{\hbar^2}{2m^*}(k_x^2 + k_y^2),$$

where m^* is the electron effective mass, k_x and k_y are the wave-vectors parallel to the interface and E_n are the electric quantum levels arising from the confinement in the z-direction (growth direction). The effective Bohr radius in GaAs is $a_0^* = 9.79$ nm which is much larger than the lattice constant of the materials (5.65 Å for GaAs). The electrons' wavefunctions "experience" an average lattice potential and the effect of the surrounding lattice is included in the effective mass ($m^* = 0.067m_e$ for GaAs, m_e is the free-electron mass). The dielectric constant is also changed, $\epsilon_r = 12.5$ for GaAs, but is equal to 1 in vacuum. It should be noted that SI-units are always used in this thesis when expressing physical quantities.

There are several ways to create quantum dots from the 2DEG. One way is to place metallic gates on top of the heterostructure and apply a voltage to them such that a small island of electrons is formed [3]. Such a system is called a *quantum dot*. The motion of the electrons is confined in all three dimensions, leading to a discrete energy spectrum, in that sense, the system is zero-dimensional. This kind of quantum dot is used in tunneling measurements.

Excitation energies for transitions between the discrete quantum dot levels are in the range of a few meV; the far-infrared range of the electromagnetic spectrum. In FIR absorption measurements, the signals are usually very weak. It is therefore necessary to produce an array of many identical dots, to obtain as strong signals as possible. This is done with holographic lithography and etching processes.

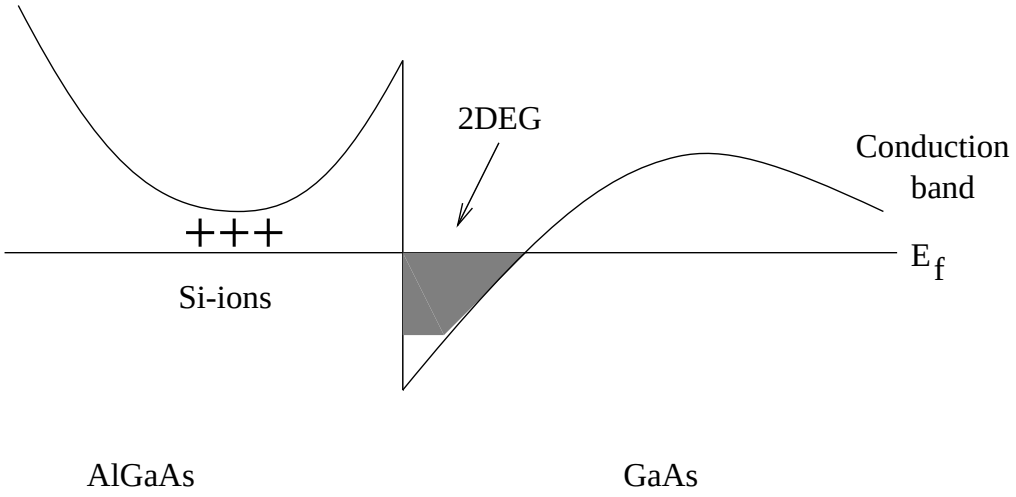

Figure 2.2: Schematic conduction bandedge profile of the $Al_xGa_{1-x}As/GaAs$ heterostructure doped with silicon.

2.2 Realization of quantum dots for FIR measurements

To produce arrays of many identical dots, holographic lithography is used. Essentially, it is done by placing, on top of the AlGaAs, a layer of material sensitive to an incident light beam; a so-called photoresist. A schematic picture of the holographic lithography process is shown in Fig. 2.3. A laser-beam is broadened and parallelized through a lens. It is then directed in two directions with a beam-splitter and the two beams are reflected by mirrors on each side onto the sample. Then, the photoresist is developed, removing stripes where the two beams interfered constructively and

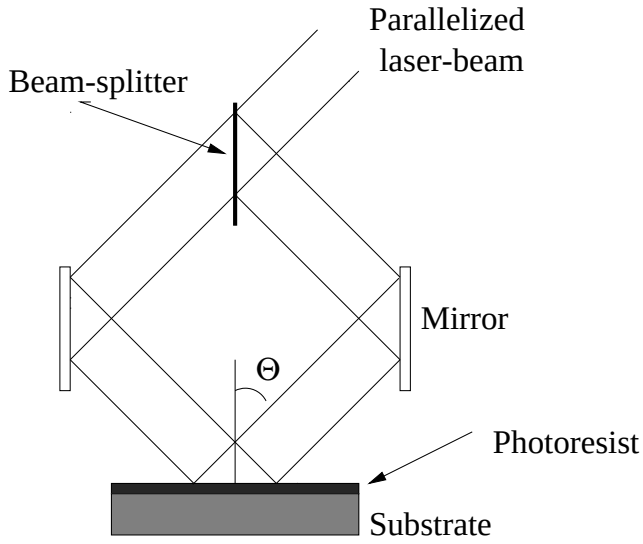

Figure 2.3: The holographic lithography process [5, 6].

light shone on the resist. The period of the array is determined by the angle Θ and the wavelength of the light. In forming a dot-structure, the sample is turned 90° and the same process is performed. The substrate is then etched and shielded with an isolating layer, f. ex. SiO_2. Fig. 2.4 shows one type of a quantum dot array. Adjustment of applied voltage, V_G, varies the number of electrons in each dot [5]. At low temperatures, the number of electrons in each dot is stabilized, since the energy required to add/remove one electron is much larger than the typical energy provided by thermal fluctuations ($\sim k_B T$), due to the electrons' mutual Coulomb interaction. The dot array in Fig. 2.4 is a combination of two methods, deep-mesa-etching and field-effect confinement. In deep-mesa-etched dots, the electrons are confined to the middle of each dot by the positively charged Si-donors and negatively charged surface states. In field-effect confined dots, there is no etching into the substrate and a layer of a semitransparent gate is placed on the photoresist structure. A negative gate voltage confines the electrons under the photoresist dots and varies the number of electrons [7].

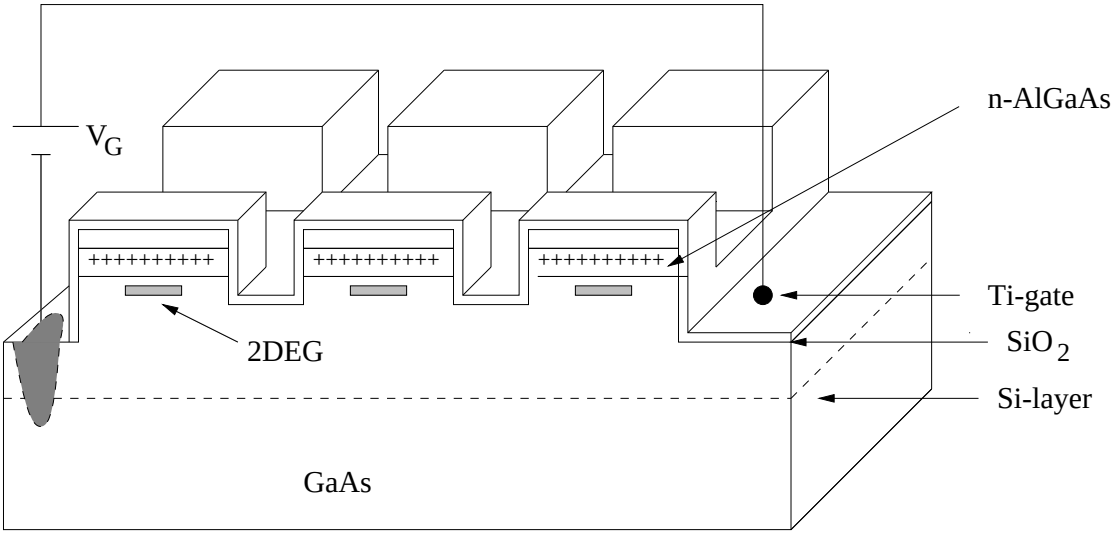

Figure 2.4: Schematic figure of a gated, deep-mesa-etched quantum dot array [5, 6].

- **Circular quantum dots**: To form circular dots, the sample is exposed to light for equally long times in each direction of the sample.
- **Elliptic quantum dots:** The sample is exposed to light for different times in the two directions of the sample. The proportion of times gives the proportion between the major and minor axes of the dots.
- **Square quantum dots:** Dots with square symmetry can be made by an anisotropic plasma-etching [8].

For FIR absorption of quantum dots, not only the resonance energies are essential. The wavelength of FIR light is much larger than the diameter of each dot, such that the electric field experienced by it is spatially constant. For harmonic quantum dots (i. e. electrons confined by a harmonic potential), the generalized Kohn theorem then has important consequences. It states that FIR light only couples to the dots' center-of-mass motion. This is formulated in the next section.

2.3 Kohn's theorem

The energy levels of a free electron in two dimensions in a (perpendicular) magnetic field (of magnitude B) are the Landau levels [9]

$$E_n = \left(n + \frac{1}{2}\right)\hbar\omega_c, \qquad n = 0, 1, \ldots$$

and

$$\omega_c = \frac{eB}{m^*}$$

is the cyclotron frequency. Classically, the electrons move under the influence of the perpendicular magnetic field in circles with the cyclotron frequency ω_c. The original Kohn theorem (by the Nobel laureate Walter Kohn) states that the light absorption of a translationally invariant two-dimensional electron gas is unaffected by the electron-electron interaction U,

$$U = \sum_{\substack{i,j \\ i \neq j}} u(\mathbf{r}_i - \mathbf{r}_j). \tag{2.1}$$

In this case, the absorption is always at the cyclotron frequency, ω_c [10].

2.3.1 The generalized Kohn theorem

Isotropic harmonic quantum dots

The generalized Kohn theorem includes electrons in circular quantum dots described by a circular parabolic (isotropic harmonic) confinement potential subject to far-infrared radiation [1, 2, 11, 12, 13]. The total Hamiltonian for the electrons in such a quantum dot is

$$H = \frac{1}{2m^*} \sum_{i=1}^{N_s} (\mathbf{p}_i + e\mathbf{A}_i)^2 + \frac{1}{2} m^* \omega_0^2 \sum_{i=1}^{N_s} \mathbf{r}_i^2 + \frac{1}{2} \frac{e^2}{4\pi\epsilon_r\epsilon_0} \sum_{i \neq j} \frac{1}{|\mathbf{r}_i - \mathbf{r}_j|} \qquad \text{(e>0)}, \tag{2.2}$$

where we have the kinetic, confinement and interaction term, respectively. ω_0 is the confinement frequency, $-e$ the electron charge, N_s the number of electrons in the dot, ϵ_r is the dielectric constant and ϵ_0 the permittivity constant. The wavelength of FIR radiation ranges between 50 μm and a millimeter and the diameter of a quantum dot is typically 50-500 nm. Each dot experiences therefore a spatially constant electric field. Assuming that it is harmonic in time, its interaction with the electrons is described by the Hamiltonian

$$H' = -e \sum_{i=1}^{N_s} \mathbf{E}^{ext} \cdot \mathbf{r}_i e^{-i\omega t} \tag{2.3}$$

$$= Q\mathbf{E}^{ext} \cdot \mathbf{R} e^{-i\omega t}, \tag{2.4}$$

where

$$\mathbf{R} = \frac{1}{N_s} \sum_{i=1}^{Ns} \mathbf{r}_i$$

is the coordinate of the center-of-mass and

$$Q = -eN_s$$

is the total charge. The Hamiltonian can be rewritten as [1]

$$H = \frac{1}{2M}(\mathbf{P} + Q\mathbf{A})^2 + \frac{1}{2}M\omega_0^2 R^2 + H_{rel}, \tag{2.5}$$

where $\mathbf{P} = \sum_{i=1}^{N_s} \mathbf{p}_i$, $\mathbf{A}$ is the vector potential of the center-of-mass and $M = N_s m^*$ is the total mass of the electrons. H_{rel} is a function of only the relative coordinates and includes the effects of the interaction. H_{rel} and H_{cm} commute. H' is expressed in terms of the center-of-mass coordinate $\mathbf{R}$, but does not depend on the relative coordinates. Therefore it commutes with H_{rel}. H' does however not commute with H_{cm}. As a consequence, FIR excites only the center-of-mass motion; *the interaction is unaffected by it.* H_{cm} has exactly the same form as the Hamiltonian of a single particle. Furthermore, absorption occurs at the same frequencies as for a single electron

$$\omega_\pm = \frac{1}{2}(\Omega \pm \omega_c), \tag{2.6}$$

where

$$\Omega = \sqrt{\omega_c^2 + 4\omega_0^2},$$

since ω_c depends only on the charge-to-mass ratio

$$-\frac{e}{m^*} = \frac{Q}{M}.$$

Anisotropic harmonic quantum dots

The generalized Kohn theorem has been extended to include also parabolic confinement potentials with arbitrary unequal confinement frequencies, ω_x, ω_y and ω_z in the three directions [2, 13]. A general dispersion equation for the absorption of electrons in a tilted magnetic field is then

$$\begin{aligned} \omega^6 - \omega^4(\omega_c^2 + \omega_x^2 + \omega_y^2 + \omega_z^2) \\ +\omega^2[\omega_c^2(\omega_x^2 \sin^2\theta\cos^2\psi + \omega_y^2 \sin^2\theta \sin^2\psi + \omega_z^2\cos^2\theta) \\ +(\omega_x^2\omega_y^2 + \omega_z^2\omega_x^2 + \omega_y^2\omega_z^2)] - \omega_x^2\omega_y^2\omega_z^2 = 0, \end{aligned}$$

where (θ, ψ) are the angles in spherical coordinates defining the direction of the magnetic field. In the case of a magnetic field perpendicular to the two-dimensional plane ($\theta = 0°$) and an elliptic confinement potential in the two directions,

$$V_{\text{conf}} = \frac{1}{2}m^* \sum_{i=1}^{N_s}(\omega_x^2 x_i^2 + \omega_y^2 y_i^2),$$

the third degree of freedom is frozen out and the eigenmodes are solutions to

$$\omega^4 - \omega^2(\omega_x^2 + \omega_y^2 + \omega_c^2) + \omega_x^2\omega_y^2 = 0. \tag{2.7}$$

The eigenfrequencies are then

$$\omega_{\pm}^2 = \frac{\omega_x^2 + \omega_y^2 + \omega_c^2 \pm [\omega_c^4 + 2\omega_c^2(\omega_x^2 + \omega_y^2) + (\omega_x^2 - \omega_y^2)^2]^{1/2}}{2} \tag{2.8}$$

and ω_x and ω_y are the resonances at $B = 0$. Equation (2.6) is a special case of eq. (2.8) with $\omega_x = \omega_0 = \omega_y$. Figure 2.5 shows the resonance frequencies, $\omega_{\pm}$, given by eq. (2.6) and (2.8) as a function of the external magnetic field.

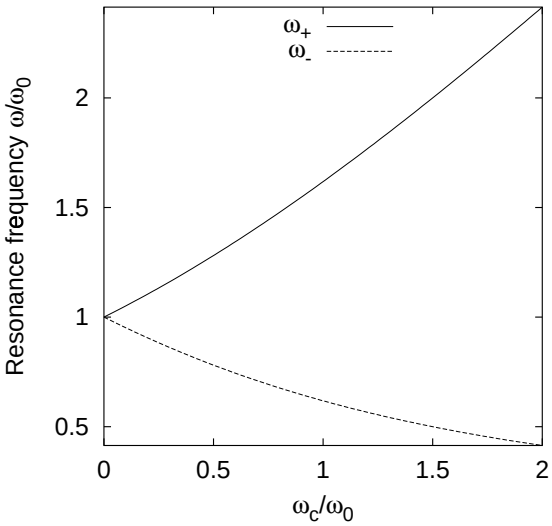

(a) FIR resonances of a parabolically confined quantum dot.

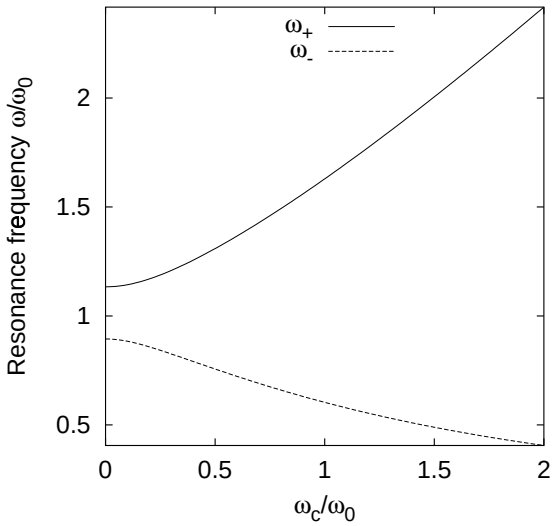

(b) FIR resonances of an elliptic dot with $\omega_x/\omega_0 = 1.05$ and $\omega_y/\omega_0 = 0.95$ (eq. (2.8)).

Figure 2.5: FIR resonances of an isotropic (a) and an anisotropic (b) harmonic quantum dot.

The energy spectrum and eigenfunctions of a single electron circular quantum dot in a perpendicular magnetic field, described by an isotropic harmonic confinement potential, has been known since the late twenties [14, 15]. In the next chapter, the properties of such an electron system will be discussed. An addition of a multipole expansion in two dimensions to the confinement potential will break the circular symmetry. A solution method to Schrödinger's equation will be presented and energy spectra will be calculated for elliptic and square symmetric confinement potentials. Effects of the deviation confinement on energy spectra will be discussed.

Chapter 3

Quantum dot hydrogen

The man-made confinement potential and the discreteness of quantum dot energy spectra have given rise to the name *artificial atoms* for quantum dots. For electrons in circular quantum dots, an isotropic harmonic confinement potential has proven to be a realistic approximation. The energy spectrum and wavefunctions of the associated Hamiltonian were found by Fock in 1928 [14] and Darwin in 1930 [15] for a single electron in a perpendicular magnetic field (section 3.1). When a multipole expansion (in two dimensions) is added to the circular parabolic confinement potential, the circular symmetry is broken. The influence of the multipole expansion on energy spectra is discussed for elliptic and square type confinement, in view of selection rules and first order perturbation theory. A solution method to the associated Schrödinger equation is sketched.

3.1 An isotropic harmonic quantum dot in a perpendicular magnetic field

The Hamiltonian for a single electron, of mass m^*, moving freely in an external magnetic field, is given by

$$H_0 = \frac{\hbar^2}{2m^*}\big(-i\nabla + \frac{e}{\hbar}\mathbf{A}\big)^2. \tag{3.1}$$

We assume that the electron motion is confined to two dimensions. We express the vector potential in the symmetric gauge

$$\mathbf{A} = \frac{1}{2}B(-y, x, 0),$$

where $B = |\mathbf{B}|$ and (x, y) are the Cartesian coordinates. Then,

$$\mathbf{B} = \nabla \times \mathbf{A} = (0, 0, B);$$

the external magnetic field is in the z-direction. In this gauge, the Hamiltonian (3.1) transforms into

$$H_0 = -\frac{\hbar^2}{2m^*}\big(\partial_r^2 + \frac{1}{r}\partial_r + \frac{1}{r^2}\partial_\phi^2 + \frac{i}{\ell^2}\big) + \frac{m^*\omega_c^2}{8}r^2, \tag{3.2}$$

where (r, ϕ) are the polar coordinates. The so-called magnetic length, ℓ, is given by

$$\ell^2 = \frac{\hbar}{eB}$$

and the cyclotron frequency, ω_c, by

$$\omega_c = \frac{eB}{m^*}.$$

If the circular parabolic confinement potential, $V_{\text{par}}(r, \phi) = \frac{1}{2} m^* \omega_0^2 r^2$, is added to H_0, the Schrödinger equation becomes

$$(H_0 + V_{\text{par}})\Phi = E\Phi.$$

The eigenfunctions are given by

$$\Phi_{M,n_r}(r, \phi) = \frac{1}{2^{\frac{|M|+1}{2}} a} \left(\frac{n_r!}{\pi(|M| + n_r)!} \right)^{\frac{1}{2}} \left(\frac{r}{a} \right)^{|M|} e^{-r^2/4a^2} L_{n_r}^{|M|} \left(\frac{r^2}{2a^2} \right) e^{-iM\phi}, \tag{3.3}$$

where a new characteristic length scale is formed by the magnetic length and the confinement potential

$$a^2 = \frac{\ell^2}{\sqrt{1 + 4(\frac{\omega_0}{\omega_c})^2}}. \tag{3.4}$$

$L_{n_r}^{|M|}(x)$ is the Laguerre polynomial given by

$$L_{n_r}^{|M|}(x) = \sum_{k=0}^{n_r} (-1)^k \binom{n_r + |M|}{n_r - k} \frac{x^k}{k!}. \tag{3.5}$$

The energy spectrum is

$$E_{M,n_r} = \left[n_r + \frac{|M|}{2} + \frac{1}{2} \right] \hbar\Omega - \frac{1}{2} M \hbar \omega_c, \tag{3.6}$$

where

$$\Omega = \sqrt{\omega_c^2 + 4\omega_0^2}$$

is a characteristic confinement frequency. The relationship between the two quantum numbers M and n_r is sketched in Fig. 3.3. M describes rotation around the z-axis and is an angular momentum quantum number, but n_r is a radial quantum number.

We can use eq. (3.6) to plot the energy spectrum as a function of the external magnetic field (Fig. 3.1), a graph named after Darwin-Fock. One should especially notice the degeneracy at $B = 0$ T. This is the familiar two-dimensional harmonic

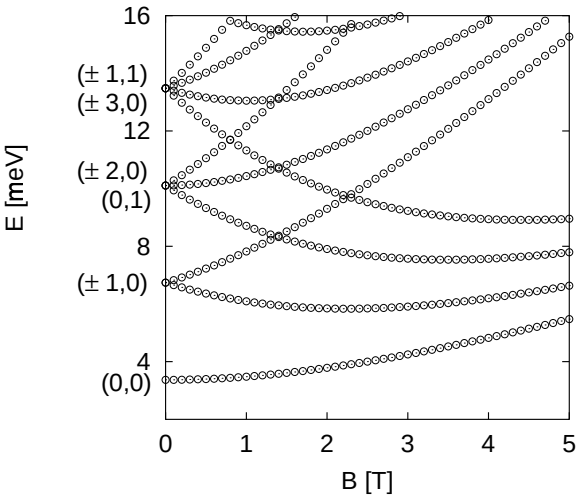

Figure 3.1: A Darwin-Fock graph of an isotropic harmonic quantum dot. The states at $B = 0$ T are labelled with (M, n_r). We use $\hbar\omega_0 = 3.37$ meV.

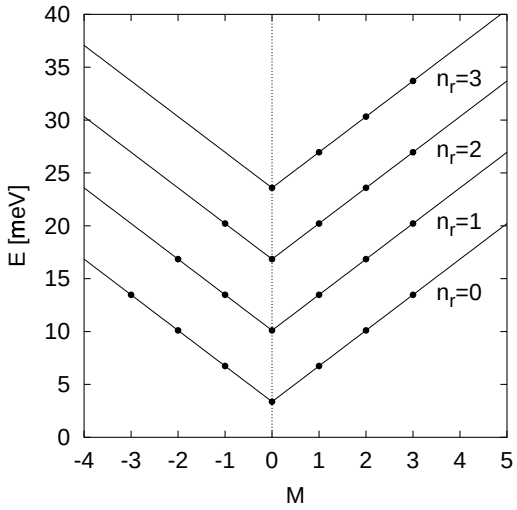

Figure 3.2: The energy levels at $B = 0$ T plotted as a function of the angular momentum quantum number, M. The quantum numbers are the same as shown in Fig. 3.3.

oscillator, a special case of eq. (3.6) with $B = 0$ and hence $\omega_c = 0$. The energy levels then fulfill the equation

$$E_{M,n_r} = (2n_r + |M| + 1)\hbar\omega_0. \tag{3.7}$$

To see the degeneracy at $B = 0$ T more explicitly, we can plot the energy (eq. (3.7)) as a function of M for given n_r (Fig. 3.2). For a given n_r the energy levels can be interpolated with lines of slope $\pm\hbar\omega_0$. As the external magnetic field increases, the lines' slope for $M < 0$ increases (becomes more negative) but for $M > 0$ the slope decreases. This lifts the degeneracy of the levels.

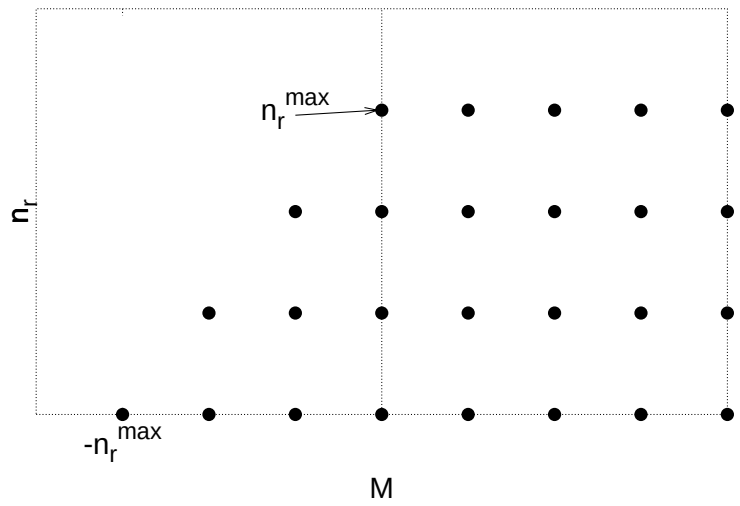

Figure 3.3: The relationship between the quantum numbers M and n_r in a truncated subspace with n_r^{max}=3 and M^{max} =4. For a given n_r, the minimum value of M is $-n_r^{max}$. The lowest value of n_r is zero.

3.2 Deviations from the circular parabolic confinement

A contribution of the form

$$V_\phi(r,\phi) = \frac{1}{2}m^*\omega_0^2 r^2 \sum_{p=1}^{p_{max}} \alpha_p \cos(2p\phi), \tag{3.8}$$

to the parabolic confinement $V_{par}(r,\phi)$ breaks the circular symmetry. This is a multipole expansion in two dimensions with high symmetry as the potential is mirror symmetric around both the x and y-axis.

3.2.1 Elliptic confinement

In the special case $\alpha_1 \neq 0$ and $\alpha_p = 0$, $p \neq 1$, one can rewrite the total confinement potential as

$$V_{\text{conf}}(x,y) = \frac{1}{2}m^*\omega_0^2\big((1+\alpha_1)x^2 + (1-\alpha_1)y^2)\big). \tag{3.9}$$

The total confinement potential then has equipotential lines of elliptic form. The ratio between the minor and major axis of an equipotential curve is then seen from eq. (3.9) to be

$$\frac{w_x}{w_y} = \sqrt{\frac{1-\alpha_1}{1+\alpha_1}}, \tag{3.10}$$

where w_x and w_y are the minor and major axis' lengths respectively (if we assume that $0 < \alpha_1 < 1$). Fig. 3.4 shows one example of an elliptic confinement potential

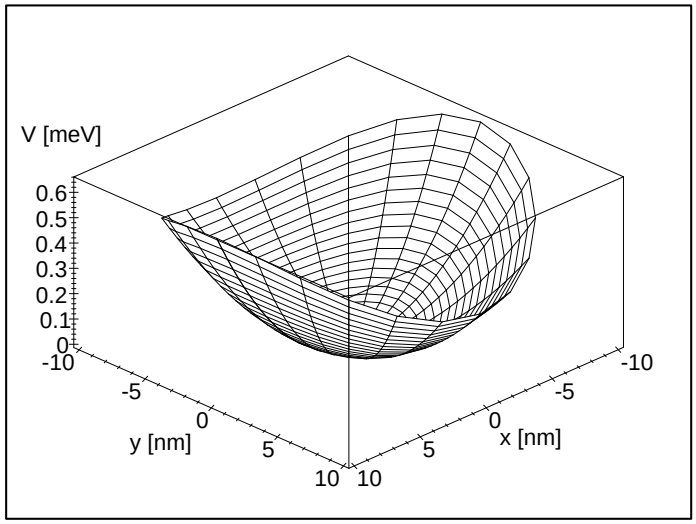

Figure 3.4: A plot of an elliptic confinement potential (eq. (3.9)). $\alpha_1 = 0.3$ and $\alpha_2 = 0.0$.

for $\alpha_1 = 0.3$. In Fig. 3.5, the equipotential lines of an elliptic confinement are shown in comparison to the equipotentials of a circular parabolic confinement. The energy spectra for $\alpha_1 = 0.1$, 0.2 and 0.4 are shown in Fig. 3.6. A comparison with Fig. 3.1 shows that the elliptic deviation lifts the degeneracy at $B = 0$ T for the circular parabolic confinement (the two-dimensional harmonic oscillator). This can be argued with first order perturbation theory, the off-diagonal matrix elements for which $\Delta M = \pm 2$ are non-zero;

$$\langle M, n_r | V_\phi | N, m_r \rangle \propto \int_0^{2\pi} d\phi e^{-i\Delta M \phi} cos(2p\phi) \qquad (\Delta M = N - M) \tag{3.11}$$

$$= \pi[\delta_{\Delta M, 2p} + \delta_{\Delta M, -2p}] \tag{3.12}$$

The corresponding states are thus coupled and the degeneracy is lifted.

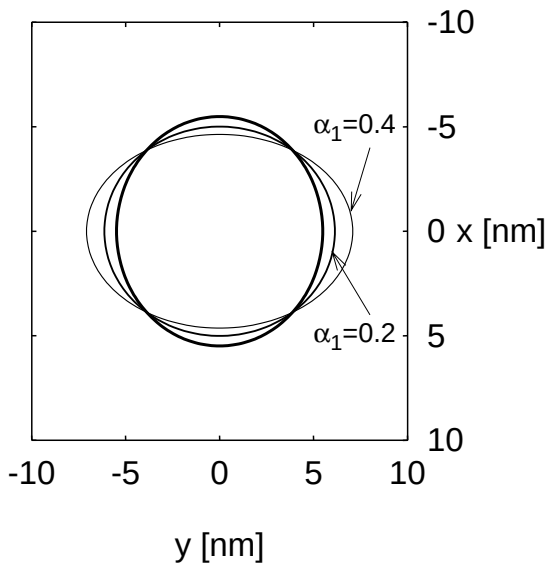

Figure 3.5: Deviation from circular parabolicity in the cases $\alpha_1 = 0.2$ and $\alpha_1 = 0.4$. The deviation increases with increasing α_1.

3.2.2 Square deviation from a circular parabolic confinement

Another special case is $\alpha_2 \neq 0$ and $\alpha_p = 0$, $p \neq 2$. This is a square symmetric deviation from the circular parabolic confinement. Fig. 3.7 shows the confinement potential in the case α_2 =0.4. The energy spectra for $\alpha_2 = 0.2$ and 0.4 are shown in Fig. 3.8. It reveals an anticrossing at $B \approx 2.3$ T. The states $|1, 0\rangle$ and $|-3, 0\rangle$ are accidentally degenerate in the circular parabolic potential. They fulfill $\Delta M = \pm 4$ and are thus coupled as eq. (3.12) shows. There is also a lifting of degeneracy at $B =$ 0 T where $\Delta M = \pm 4$. The degenerate states at $B = 0$ T fulfilling $M = \pm 1$ remain however unchanged, whereas their degeneracy is lifted in the elliptic confinement case.

3.2.3 Solution to Schrödinger's equation

We denote by $|\zeta_k\rangle$ the states for a single electron in a general confinement potential that does not necessarily have a circular symmetry. They are expanded in the Darwin-Fock basis $\{|\Phi_i\rangle\}$,

$$|\zeta_k\rangle = \sum_i c_{ki} |\Phi_i\rangle, \tag{3.13}$$

where $i := (M, n_r)$. Schrödinger's equation,

$$(H_0 + V_{\text{par}} + V_\phi)|\zeta_k\rangle = E'_k |\zeta_k\rangle$$

transforms into

$$\sum_i (H_0 + V_{\text{par}} + V_\phi)|\Phi_i\rangle = E'_k \sum_i c_{ki}|\Phi_i\rangle, \tag{3.14}$$

or

$$\sum_i \{\langle\Phi_j|(H_0 + V_{\text{par}})|\Phi_i\rangle + \langle\Phi_j|V_\phi|\Phi_i\rangle\}c_{ki} = E'_k c_{kj} \tag{3.15}$$

$$\Longrightarrow \quad \sum_i \{E_i\delta_{ij} + \langle\Phi_j|V_\phi|\Phi_i\rangle\}c_{ki} = E'_k c_{kj}, \tag{3.16}$$

where E_i is an energy level of $(H_0 + V_{\text{par}})$, see eq. (3.6). Schrödinger's equation has thus been transformed into an infinite set of algebraic eigenvalue equations (3.16). The solution can be approximated by truncating the basis. In order to solve the matrix equation (3.16), the quantum numbers (M, n_r), within the truncated basis, are mapped with a bijective mapping to a single number $1 \leq i \leq i^{max}$, where i^{max} represents the dimension of the basis $\{|\Phi_i\rangle\}$ (and the number of eigenvalue equations). The dependence of M and n_r on each other is shown in Fig. 3.3. The bijective mapping $\iota : A \to D$ with $D \subset \mathbf{N} \setminus \{0\}$ and $A \subset \mathbf{Z} \times \mathbf{N}$,

$$\iota(M, n_r) = \sum_{j=0}^{n_r-1} (N - j) + 1 + M + n_r^{max} - n_r, \tag{3.17}$$

where $N = n_r^{max} + M^{max} + 1$ is the number of quantum numbers in the first row $(n_r = 0)$, fulfills the requirements. The sum counts the quantum numbers in rows $n_r = 0$ up to $(n_r - 1)$. The minimum value of M for a given value of n_r is $(-n_r^{max} + n_r)$. With a few algebraic steps, the mapping can be written as

$$\iota(M, n_r) = n_r\big(n_r^{max} + M^{max} + \frac{1 - n_r}{2}\big) + n_r^{max} + M + 1. \tag{3.18}$$

The mapping fulfills $\iota(M^{min} = -n_r^{max}, 0) = 1$. It is strictly increasing and i increases by unity when

- M is increased by 1 within the same n_r,
- going from (M^{max}, n_r) to the minimum M in $(n_r + 1)$; $(-n_r^{max} + (n_r + 1))$.

The solution to eq. (3.16) then gives the energy levels (eigenvalues) $\{E'_k\}_{k=1}^{i^{max}}$. For a given k, the vector $(c_{ki})_{i=1}^{i^{max}}$ gives the expansion coefficients of $|\zeta_k\rangle$ in the Darwin-Fock basis $\{|\Phi_i\rangle\}$.

The matrix element of the deviation potential, $\langle\Phi_j|V_\phi|\Phi_i\rangle$, is evaluated in Appendix A.1. In the case of a circular parabolic confinement, $c_{ki} = \delta_{ki}$. The wavefunctions are the basis functions (3.3) and the quantum numbers M and n_r are well defined. However, for the general confinement, where the contribution V_ϕ in eq. (3.8)

has been added to the circular parabolic confinement, and $\exists i$ such that $\alpha_i \neq 0$, M and n_r are no longer defined for a given state. This is crucial as we will see later; *we have allowed for mixing of all M and n_r.* The mixing of M means in other words that there is no longer conservation of angular momentum.

In this chapter, we have studied one electron systems subject to circular parabolic, elliptic and square symmetric confinement potentials and the influence of the deviation confinement on the energy spectra. For many electron quantum dots, their mutual Coulomb interaction is of great importance, since the typical Coulomb energy, $e^2/(4\pi\epsilon_r\epsilon_0 a)$, is of the order of 10 meV. The deviation confinement potential, V_ϕ, is of a very general kind and solving Schrödinger's equation requires mixing of all quantum numbers (M, n_r) within the truncated basis. This increases largely the running time of programs when the Coulomb interaction has been taken into account. In the following chapter, we will investigate the ground state properties of 2-3 interacting electrons in quantum dots. To include the Coulomb interaction, several many body approximations exist, such as the Hartree-Fock approximation (HFA) or the local density approximation (LDA). Here, the Hartree approximation will be used.

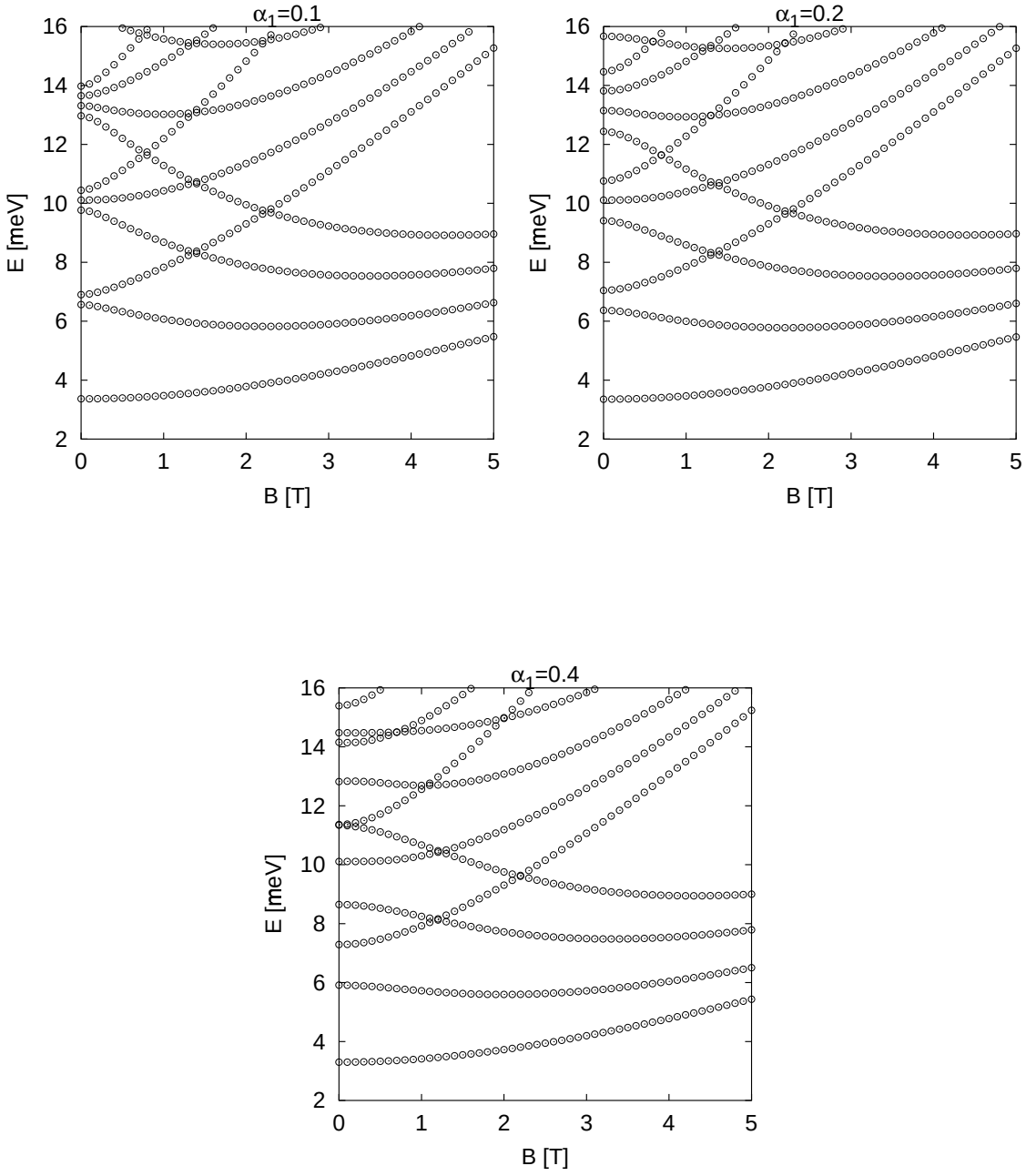

Figure 3.6: Energy spectra for an elliptic confinement. The deviation to the circular confinement, V_ϕ, lifts the degeneracy at $B = 0$ T from the circular parabolic case (Fig. 3.1). First order perturbation shows that the states for which $\Delta M = \pm 2$ are coupled. Note also the accidental degeneracy at $B = 0$ T, $E \approx 11.3$ meV for $\alpha_1 = 0.4$.

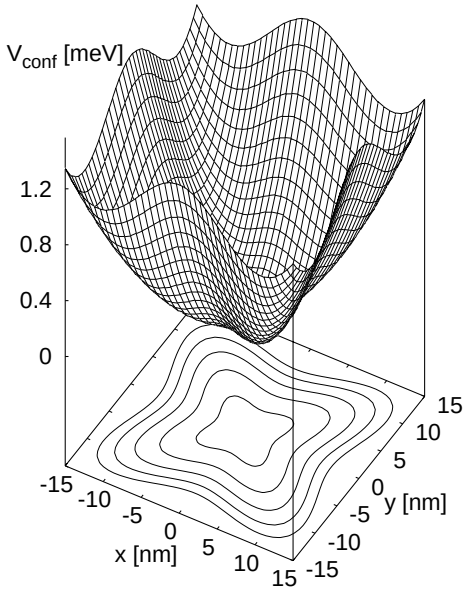

Figure 3.7: The "square" confinement potential in the case α_2 =0.4.

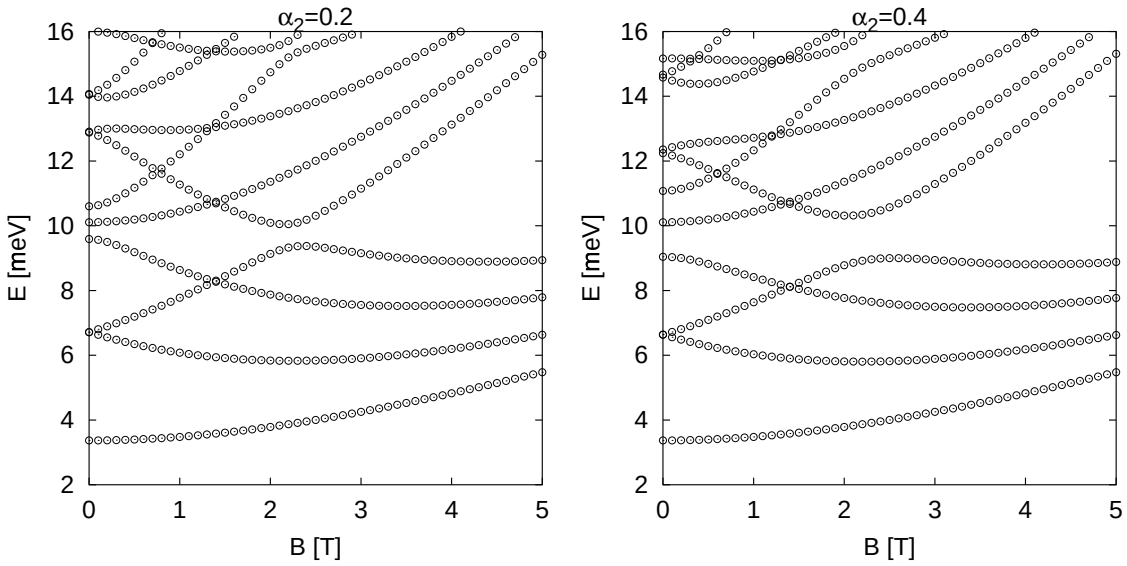

Figure 3.8: Energy spectra for a square type confinement. The angular part of V_ϕ, $\cos(4\phi)$, couples states for which $\Delta M = \pm 4$. An anticrossing thus occurs at $B \approx 2.3$ T due to coupling of $|-1,0\rangle$ and $|+3,0\rangle$, but these states are accidentally degenerate for this magnetic field in the circular parabolic potential (Fig. 3.1). Also, the $\Delta M = \pm 4$ coupling lifts the degeneracy of states at $B = 0$ T.

Chapter 4

Many electron quantum dots

For more than one electron occupying the quantum dot, their mutual Coulomb interaction becomes important and needs to be included. The typical Coulomb energy, $e^2/(4\pi\epsilon_0\epsilon_r a)$, is of the order of 10 meV, whereas the confinement energy ($\hbar\Omega$) is typically of the same order. In this chapter, the influence of the Coulomb interaction on the quantum dot's charge distribution is studied in the case of harmonic and square symmetric 2-3 electron quantum dots. The interaction is included within the Hartree approximation. It is a mean-field approximation, which consists of writing an effective Hamiltonian for each electron and solving the associated (nonlinear) Schrödinger equation. The nonlinearity of the equation and the strength of the Coulomb potential require it to be solved by iteration self-consistently. Electron densities are shown for circular parabolic, elliptic and square confinement potentials in zero magnetic field. For elliptic and square dots, the densities are very different for 2 and 3 electrons. This must be explained by a mixing of M, which is not present in the strictly harmonic case.

4.1 The Hartree approximation

The Coulomb interaction is included with the Hartree approximation (see [16]). In this approximation, the effective Hamiltonian for each electron is written as

$$H = \frac{\hbar^2}{2m^*}\Big(-i\nabla + \frac{e}{\hbar}\mathbf{A}\Big)^2 + V_{\text{conf}}(\mathbf{r}) + V_H(\mathbf{r}) \tag{4.1}$$

and Schrödinger's equation,

$$H|\Psi_\alpha\rangle = \varepsilon_\alpha|\Psi_\alpha\rangle, \tag{4.2}$$

is solved. $V_H(\mathbf{r})$ is the classical Coulomb potential established by the total electron charge density. It is called the Hartree potential and is related to the electron density via Poisson's equation;

$$\nabla^2 V_H(\mathbf{r}) = -\frac{e^2}{\epsilon_0\epsilon_r} n_s(\mathbf{r}). \tag{4.3}$$

with ϵ_0 the permittivity constant and ϵ_r the dielectric constant. The solution to Poisson's equation (4.3) is

$$V_H(\mathbf{r}) = \frac{e^2}{4\pi\epsilon_r\epsilon_0}\int_{\mathbf{R}^2} d\mathbf{r}'\frac{n_s(\mathbf{r}')}{|\mathbf{r}-\mathbf{r}'|} \tag{4.4}$$

with

$$-\frac{1}{4\pi|\mathbf{r}-\mathbf{r}'|}$$

the Green's function for the Laplacian, ∇^2, in $\mathbf{R}^3$. The electron density is given by

$$n_s(\mathbf{r}) = \sum_\alpha f(\varepsilon_\alpha)\left|\Psi_\alpha(\mathbf{r})\right|^2, \tag{4.5}$$

where for thermal equilibrium

$$f(\varepsilon_\alpha) = \left[\exp\Big(-\frac{\varepsilon_\alpha-\mu}{k_BT}\Big)+1\right]^{-1} \tag{4.6}$$

is the Fermi distribution with k_B the Boltzmann constant and T the temperature of the system. The chemical potential, μ, is determined by fixing the number of electrons, N_s, in the dot;

$$N_s = \sum_\alpha f(\varepsilon_\alpha). \tag{4.7}$$

The interacting states $\{|\Psi_\alpha\rangle\}$ are expanded in the basis $\{|\Phi_i\rangle\}$ previously defined by eq. (3.3),

$$\Phi_{M,n_r}(r,\phi) = \frac{1}{2^{\frac{|M|+1}{2}}a}\Big(\frac{n_r!}{\pi(|M|+n_r)!}\Big)^{\frac{1}{2}}\Big(\frac{r}{a}\Big)^{|M|}e^{-r^2/4a^2}L_{n_r}^{|M|}\Big(\frac{r^2}{2a^2}\Big)e^{-iM\phi}, \tag{4.8}$$

where $i := (M, n_r)$ and a is the natural length scale defined earlier (3.4). We write[1]

$$|\Psi_\alpha\rangle = \sum_i c_{\alpha i}|\Phi_i\rangle. \tag{4.9}$$

In the same way as in eq. (3.16), this yields a matrix equation

$$\sum_i\{E_i\delta_{ij} + \langle\Phi_j|V_\phi|\Phi_i\rangle + \langle\Phi_j|V_H|\Phi_i\rangle\}c_{\alpha i} = \varepsilon_\alpha c_{\alpha j}. \tag{4.10}$$

Equations (4.2), (4.4) and (4.5) constitute the Hartree equations. They are summarised in equation (4.10). This matrix equation is however very different from eq. (3.16). It is nonlinear with respect to the basis $\{|\Phi_i\rangle\}$, since V_H includes multiples of the form $\Phi_i^*\Phi_j$ via the electron density (4.5). This nonlinearity, along with the relative strength of the Coulomb interaction compared to kinetic energy terms, requires this matrix equation to be solved iteratively until a self-consistent solution is obtained. The iteration procedure is described in section 4.2.

[1]Note that Greek letters are used for the interacting energy states but Arabic letters in the non-interacting case. Also, Φ and ζ denote non-interacting wavefunctions, whereas Ψ denotes the interacting wavefunctions.

4.2 The iteration process

In this thesis work, a majority of the calculations has been performed analytically. Due to the mixing of all quantum numbers within the truncated basis, program running time is very long compared to running time for a circular parabolic confinement when (M, n_r) are well defined. The analytic calculations reduce of course the numerical analysis required and thus increase the program running speed as much as possible. It was possible here to evaluate the matrix elements $\langle \Phi_j | V_H | \Phi_i \rangle$ analytically (Appendix A.2) and thus is was straight forward to perform the self-consistent calculations by mixing the matrix elements. In the n-th iteration, matrix elements were mixed according to

$$H_{ij} = (H_0 + V_{\text{conf}})_{ij} + \lambda(\alpha V_{H,ij} + (1-\alpha)(\beta V_{H,ij}^{old} + (1-\beta)V_{H,ij}^{old,old}), \tag{4.11}$$

with α =0.5 and β =0.7. $V_{H,ij}^{old}$ are the matrix elements calculated in iteration (n-1) and $V_{H,ij}^{old,old}$ in iteration (n-2). The procedure for the Hartree iteration is shown schematically in Figure 4.2. The convergence was calculated, using the norm

$$\|V_H - V_H^{old}\| = \frac{1}{i^{max}} \sum_{i=1}^{i^{max}} \sum_{j=1}^{i^{max}} \sqrt{\frac{(V_{H,ij} - V_{H,ij}^{old})^2}{V_{H,ij}^2 + \epsilon}}. \tag{4.12}$$

ϵ was added in the denominator to avoid division by zero, chosen here to be $\epsilon = 10^{-3}$. The norm was chosen such that the "distance" between the unity matrix and the null matrix is equal to 1 (if ϵ is not taken into account). When the criterium

$$\|V_H - V_H^{old}\| < d = 10^{-3} \tag{4.13}$$

was reached, λ was increased;

$$\lambda \to \eta\lambda, \qquad \eta = 1.2, \tag{4.14}$$

and so on. Each time λ is increased, the system experiences 20% more of the interaction. It is then allowed to accustom itself to this interaction before λ is increased again.

Such mixing of matrix elements is quite unusual, but was straightforward here, since the goal was to perform as much of the work analytically as possible. It was necessary, in order to speed up the program running time as much as possible. In general, when the problem is of a less general kind, it is custom to mix instead the electron density or the Hartree potential, where these have been evaluated numerically. In such cases, the time required for analytic evaluation of Hartree matrix elements has been considered to largely exceed the time required for numerical analysis and program running time.

Figure 4.1 shows convergence for an elliptic confinement ($\alpha_1 = 0.4$) for 2 and 3 electrons and $B = 0.1$ T. For the higher values of λ, the convergence is no longer

exponentially decreasing within one λ and there appear "feedbacks" which become more pronounced when the electron number is increased (occupation of higher energy levels for the same basis). This appeared even more pronounced if $V_H^{old,old}$ was taken out of the mixing. The matrix elements seem much more sensitive to changes than the density or the Hartree potential. The latter two are mixed according to

$$X^{new} = \lambda X + (1 - \lambda) X^{old},$$

where X denotes either the density or the Hartree potential. X is calculated in iteration n, X^{old} in iteration $(n-1)$ and λ is always kept at the same value. Such a mixing would result in an exponential convergence all the way through.

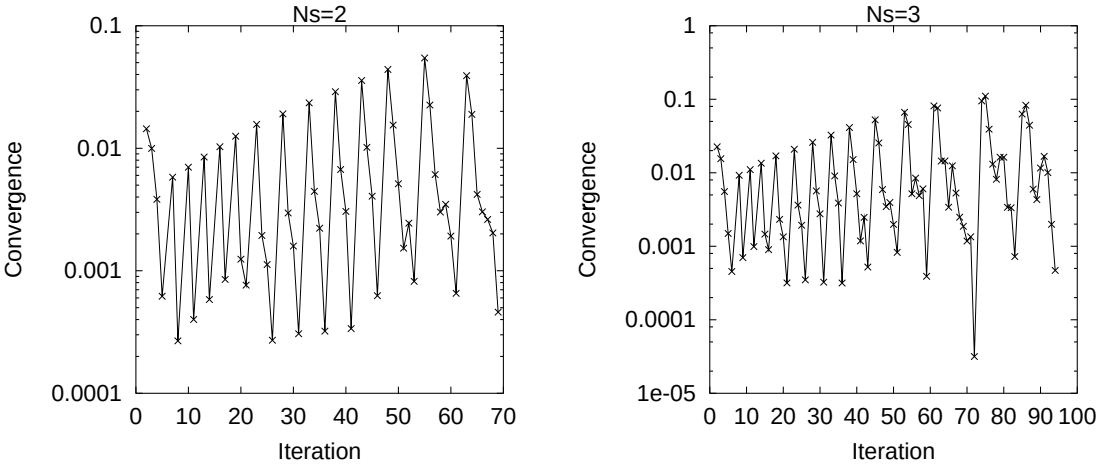

Figure 4.1: An example of convergence for $\alpha_1 = 0.4$ and $\alpha_2 = 0.0$. $M^{max} = 3$, $n_r^{max} = 3$ and $B = 0.1$ T. The peaks arise when λ is increased. The system is then allowed to relax until convergence is reached and then λ is increased again.

4.3 Results

When the energy states, ε_α, and the corresponding eigenvectors, $\mathbf{c}_\alpha = (c_{\alpha i})_{i=1}^{i^{max}}$, have been obtained, the electron density can be evaluated with equation (4.5). Electron densities are shown here in the cases

$\alpha_1 = 0.0$	and	$\alpha_2 = 0.0$	(Fig. 4.3),
$\alpha_1 = 0.4$	and	$\alpha_2 = 0.0$	(Fig. 4.4),
$\alpha_1 = 0.0$	and	$\alpha_2 = 0.4$	(Fig. 4.5).

4.3.1 Circular parabolic confinement

Fig. 4.3 shows the electron densities for a circular parabolic confinement potential ($\alpha_1 = 0.0$ and $\alpha_2 = 0.0$). For three electrons, there appears a circle in the density which is much less clear for the two electron case. This difference can be explained with aid of Fig. 3.2. The occupied states are $(M, n_r) = (0, 0)$ and $(\pm 1, 0)$ for three electrons but $(0, 0)$ and *either* $(-1, 0)$ or $(1, 0)$ for two electrons. The corresponding squared moduli of the wavefunctions are

$$|\Phi_{0,0}|^2 \propto \exp(-r^2/2a^2) \tag{4.15}$$

$$|\Phi_{\pm 1,0}|^2 \propto \frac{1}{2}\left(\frac{r}{a}\right)^2 \exp(-r^2/2a^2) \tag{4.16}$$

with the same proportionality factor. There are thus equivalent contributions to the density from the $(-1, 0)$ and the $(+1, 0)$ state but there is less weight of the Gaussian $|\Phi_{0,0}|^2$ in the density of three electrons than for two electrons. This explains why the circle appears more clearly in the three electron case.

4.3.2 Elliptic confinement

Figure 4.4 shows the electron density for an elliptic confinement ($\alpha_1 = 0.4$) for two and three electrons and their energy spectra. The density for three electrons is somewhat similar to the three electron density in circular parabolic confinement. There appear however four small peaks in the "circle" of the density. It can be understood by observing that for the elliptic confinement, the surface within a given equipotential line is larger than if $\alpha_1 = 0.0$. For two electrons, two peaks occur in the density. Due to breaking of the circular symmetry, the energy spectra are shown in a single column. The angular momentum is no longer conserved and all angular momentum quantum numbers (within the truncated basis) have been mixed. The Coulomb interaction mixes M even further.

4.3.3 Square symmetric confinement

The electron densities and energy spectra for two and three interacting electrons are shown in Fig. 4.5 for $\alpha_2 = 0.4$. The two electron density shows more screening of the interaction than for three electrons. Four peaks occur in the lower figure whereas the electrons are three. There is strong M mixing due to the deviation confinement and the interaction.

In this chapter, we have studied the ground state properties of 2-3 interacting electrons in a quantum dot and shown the effect of the Coulomb interaction on the electrons' distribution. The interacting energy states, ε_α, were calculated by iteration. They are necessary to be able to calculate the power absorbed by the system, when subject to far-infrared radiation. The electrons "communicate" via

the Coulomb interaction, such that excitations of the system will be collective. In the next chapter, we will derive equations for the dielectric tensor and the power absorption, calculated with a self-consistent method in the linear response regime; the time-dependent Hartree approximation. When those are found, we're all set to find absorption spectra for various confinement potentials.

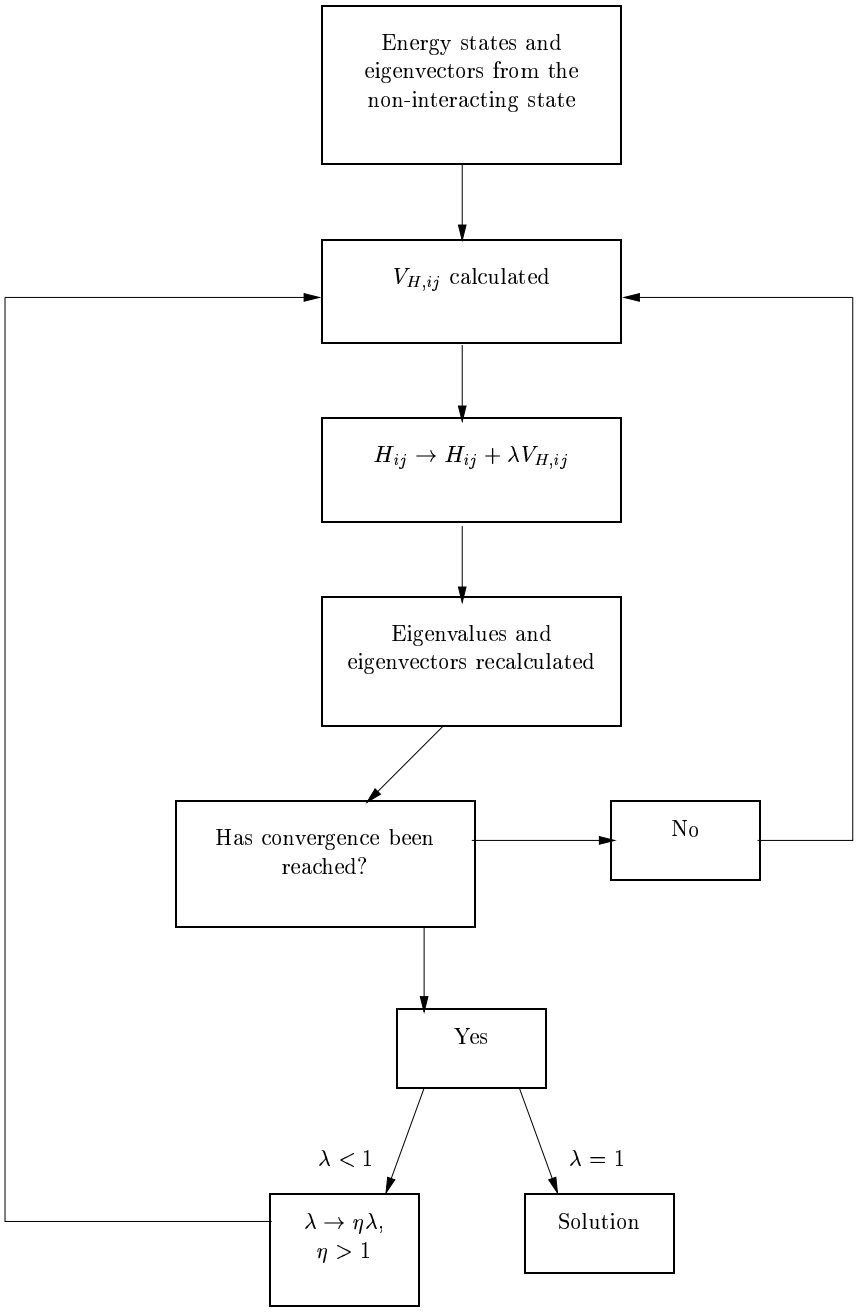

Figure 4.2: The Hartree iteration scheme.

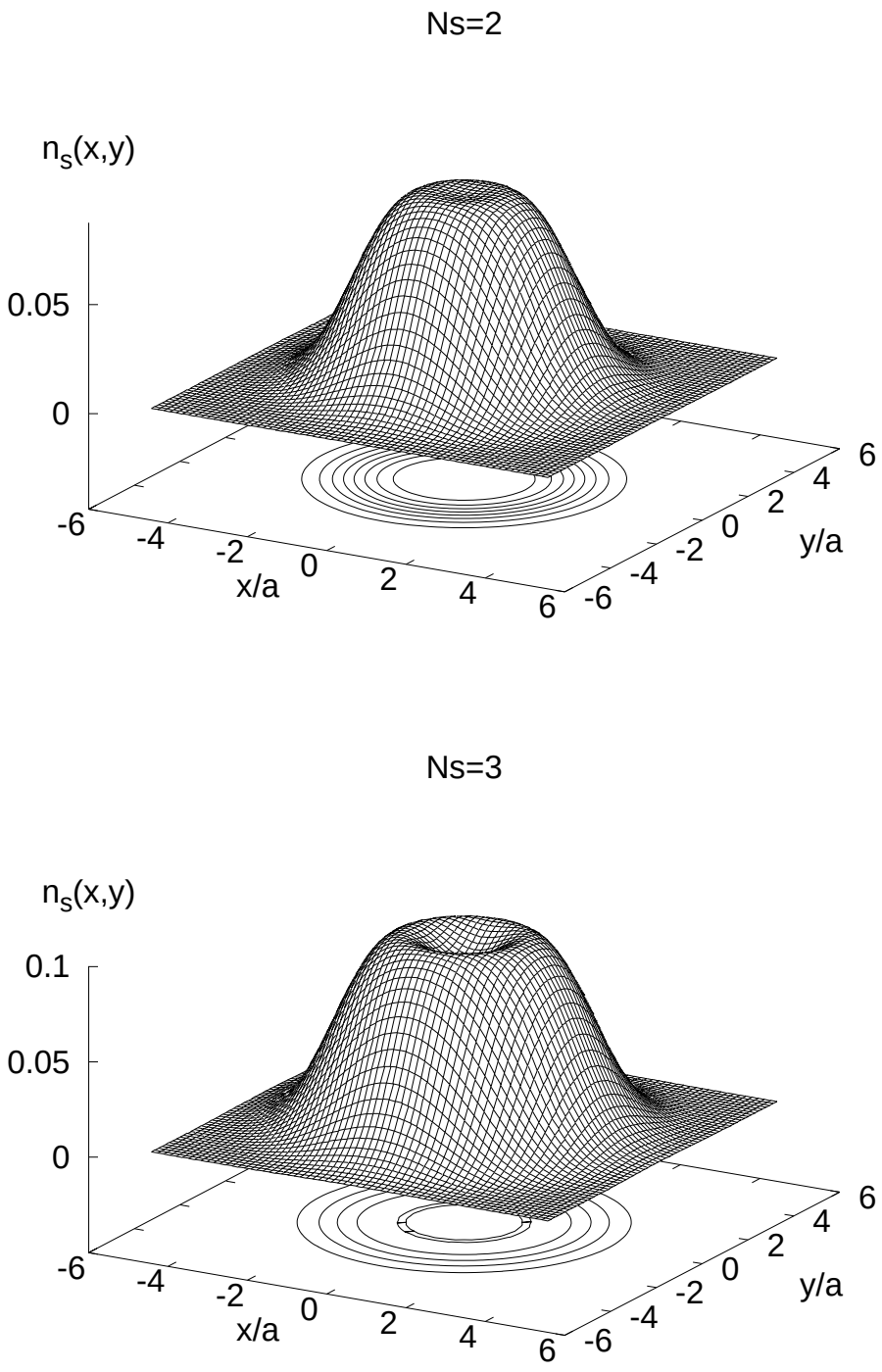

Figure 4.3: The density of two (above) and three (below) interacting electrons subject to a circular parabolic confinement potential. The circle in the three electron density arises from the wavefunction modulus properties where M and $-M$ are equivalent, and the two-fold degeneracy of the next lowest energy level. The coordinates are scaled with the magnetic length, which for $B = 0$ T is $a = 13$ nm.

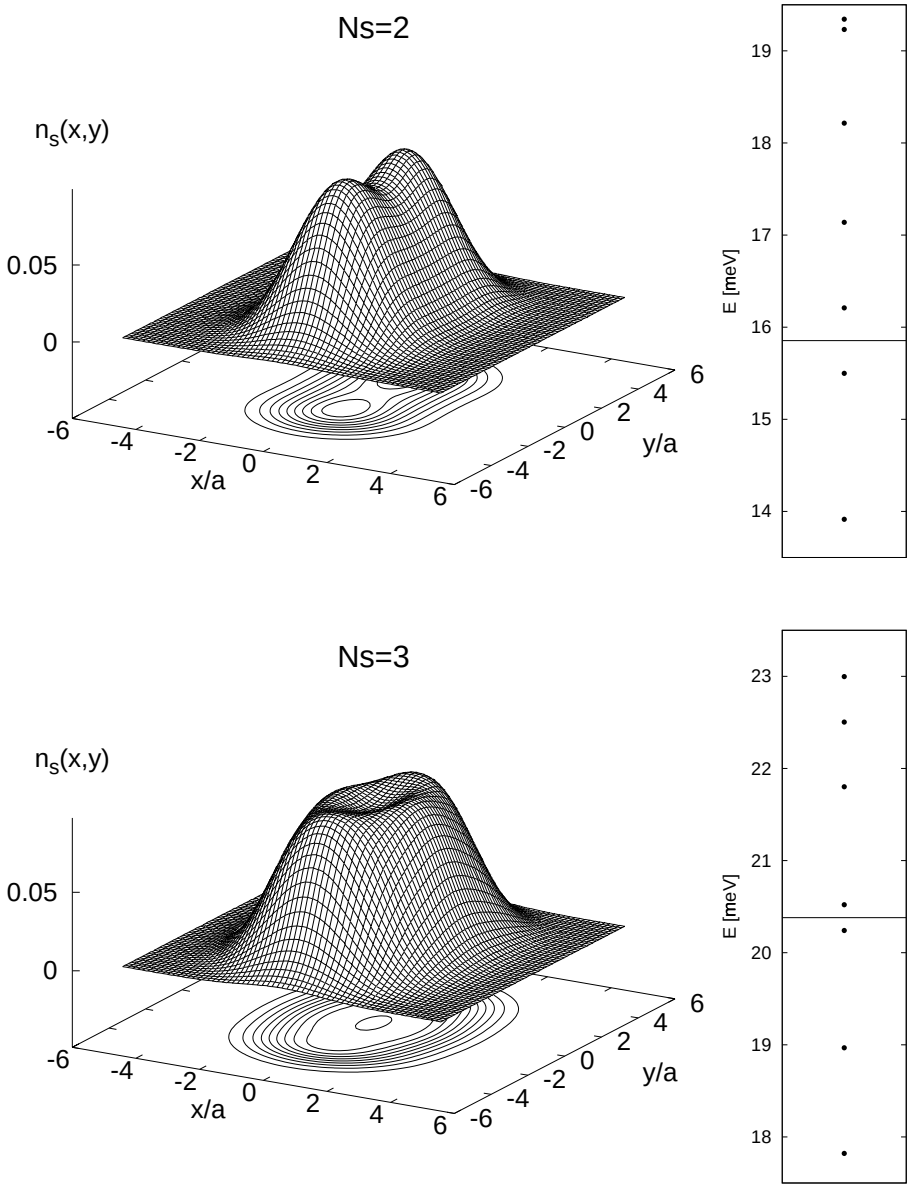

Figure 4.4: The density of two (above) and three (below) interacting electrons subject to an elliptic confinement potential with $\alpha_1 = 0.4$ and $\alpha_2 = 0.0$. The magnetic length is $a = 13$ nm.

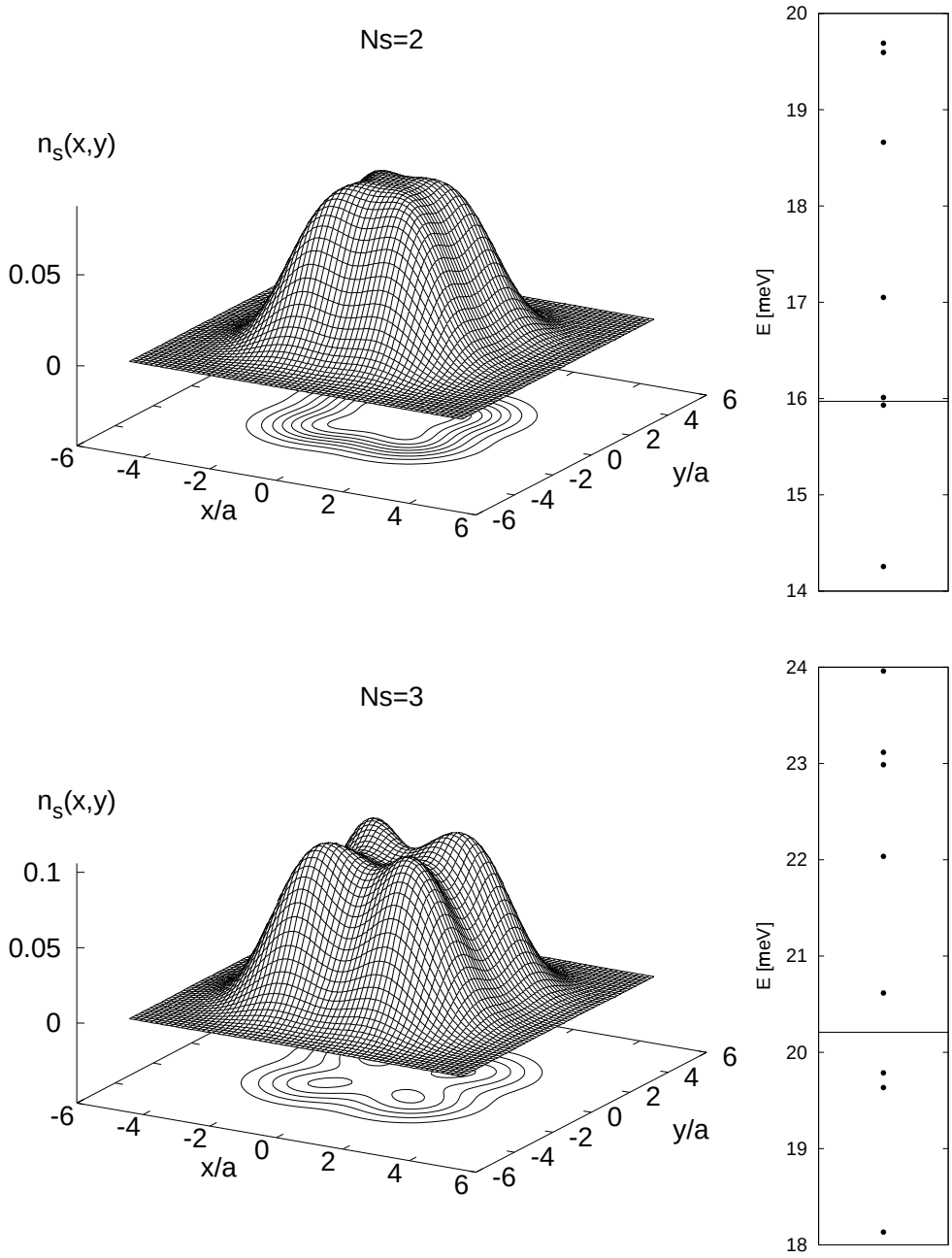

Figure 4.5: The density of two (above) and three (below) interacting electrons subject to a square symmetric confinement, $\alpha_1 = 0.0$ and $\alpha_2 = 0.4$. The magnetic length is $a = 13$ nm.

Chapter 5

Far-infrared absorption

We wish to investigate the collective excitations of a quantum dot, when subject to far-infrared irradiation. In this chapter, the FIR response of such a system will be found within the self-consistent linear response regime where the external disturbance is assumed to be small in magnitude. Expressions for the dielectric tensor (section 5.1) and the power absorption (section 5.2) will be obtained.

5.1 Dielectric response

The FIR absorption is found by a self-consistent method in the linear response regime. The approximation is called the time-dependent Hartree approximation. The self-consistency is obtained by assuming that the perturbation is not only the bare applied potential, but the total (self-consistent) electrostatic potential (see [17, 18])

$$\phi^{sc} = \phi^{ext} + \phi_H^{ind}[\phi^{sc}], \tag{5.1}$$

where ϕ_H^{ind} is the induced Hartree potential due to rearrangement of the electrons. It is a functional of ϕ^{sc} and not only ϕ^{ext}. Due to this assumption, the approximation is sometimes called a random-phase approximation (RPA). The self-consistent potential ϕ^{sc} is found as a linear response to ϕ^{ext}. The induced Hartree potential is

$$\phi_H^{ind}(\mathbf{r}, t) = -\frac{e}{4\pi\epsilon_r\epsilon_0} \int_{\mathbf{R}^2} d\mathbf{r}' \frac{\delta n_s(\mathbf{r}', t)}{|\mathbf{r} - \mathbf{r}'|}, \tag{5.2}$$

where $-e\delta n_s$ is the induced charge density.[1] The applied potential is assumed to depend harmonically on time

$$\delta V(\mathbf{r}, t) = \delta V(\mathbf{r}) \exp(-i(\omega + i\eta)t), \qquad \eta \to 0^+, \tag{5.3}$$

[1] Note that the term "potential" is used both for ϕ and $V = -e\phi$. Even if not correct, we will use it, since it can always be seen from the context what the meaning is.

where δV is assumed to be small. The density operator is written as

$$\rho(t) = \rho^0 + \delta\rho(t), \tag{5.4}$$

where

$$\rho^0 := \rho(t = -\infty) = f(H) \tag{5.5}$$

and f is the Fermi distribution. The perturbation is thus assumed adiabatically turned on. The equation of "motion" for the density operator is

$$i\hbar\dot{\rho}(t) = [H'(t), \rho(t)], \tag{5.6}$$

where

$$H'(t) = H + \delta V(t).$$

Schrödinger's equation

$$H|\Psi_\alpha\rangle = \varepsilon_\alpha|\Psi_\alpha\rangle$$

has already been solved (chapter 4) and the states, ε_α, are the interacting energy states. The equation of motion is solved in a linear approximation with respect do δV,

$$i\hbar\dot{\rho}(t) = [H, \rho(t)] + [\delta V(t), \rho^0]. \tag{5.7}$$

Since

$$\begin{aligned}\rho^0|\Psi_\alpha\rangle &= f(H)|\Psi_\alpha\rangle \\ &= f(\varepsilon_\alpha)|\Psi_\alpha\rangle \\ &=: n_\alpha|\Psi_\alpha\rangle,\end{aligned}$$

the matrix elements of the density operator fulfill the equation

$$\begin{aligned}i\hbar\delta\dot{\rho}_{\alpha\beta}(t) &= (\varepsilon_\alpha - \varepsilon_\beta)\delta\rho_{\alpha\beta}(t) + \langle\Psi_\alpha|[\delta V(t), \rho^0]|\Psi_\beta\rangle \\ &= (\varepsilon_\alpha - \varepsilon_\beta)\delta\rho_{\alpha\beta}(t) + (n_\beta - n_\alpha)\langle\Psi_\alpha|\delta V(t)|\Psi_\beta\rangle.\end{aligned} \tag{5.8}$$

This is a first order differential equation with respect to t which can easily be solved with a Fourier transformation. With the definition

$$F(t) = \frac{1}{2\pi}\int_{-\infty}^{+\infty} d\omega' e^{-i\omega' t + \eta t} F(\omega') \tag{5.9}$$

of the Fourier transform for a function F, this gives

$$\delta\rho_{\alpha\beta}(\omega') = \frac{1}{\hbar}\left\{\frac{n_\beta - n_\alpha}{\omega' + (\omega_\beta - \omega_\alpha) + i\eta}\right\} 2\pi\delta(\omega' - \omega)\langle\Psi_\alpha|\delta V|\Psi_\beta\rangle, \tag{5.10}$$

where $\omega_\alpha := \varepsilon_\alpha/\hbar$, and

$$\delta\rho_{\alpha\beta}(t) = \frac{1}{\hbar}\Big\{\frac{n_\beta - n_\alpha}{\omega + (\omega_\beta - \omega_\alpha) + i\eta}\Big\}\langle\Psi_\alpha|\delta V|\Psi_\beta\rangle e^{-i\omega t+\eta t}. \tag{5.11}$$

$\delta\rho_{\alpha\beta}(t)$ depends harmonically on t as well as $\delta V(t)$. With

$$\delta\rho_{\alpha\beta}(t) = \delta\rho_{\alpha\beta}(\omega)e^{-i\omega t+\eta t}, \tag{5.12}$$

we have thus

$$\delta\rho_{\alpha\beta}(\omega) = \frac{1}{\hbar}\Big\{\frac{n_\beta - n_\alpha}{\omega + (\omega_\beta - \omega_\alpha) + i\eta}\Big\}\langle\Psi_\alpha|\delta V|\Psi_\beta\rangle \tag{5.13}$$

$$= -\frac{e}{\hbar}\Big\{\frac{n_\beta - n_\alpha}{\omega + (\omega_\beta - \omega_\alpha) + i\eta}\Big\}\langle\Psi_\alpha|\phi^{ext}|\Psi_\beta\rangle. \tag{5.14}$$

In order to have self-consistency, ϕ^{ext} in eq. (5.14) is replaced by ϕ^{sc}, i.e. the perturbation is assumed to be the total electrostatic potential, ϕ^{sc}, rather than ϕ^{ext}. This leads to

$$\delta\rho_{\alpha\beta}(\omega) = \frac{1}{\hbar}\Big\{\frac{n_\beta - n_\alpha}{\omega + (\omega_\beta - \omega_\alpha) + i\eta}\Big\}(-e)(\langle\Psi_\alpha|\phi^{ext}|\Psi_\beta\rangle + \langle\Psi_\alpha|\phi^{ind}_H|\Psi_\beta\rangle). \tag{5.15}$$

With the definition

$$f^{\alpha\beta}(\omega) := \frac{1}{\hbar}\Big\{\frac{n_\beta - n_\alpha}{\omega + (\omega_\beta - \omega_\alpha) + i\eta}\Big\} \tag{5.16}$$

and the short hand writing

$$\phi_{\alpha\beta} := \langle\Psi_\alpha|\phi|\Psi_\beta\rangle,$$

we have

$$\delta\rho_{\alpha\beta}(\omega) = -ef^{\alpha\beta}(\omega)\phi^{sc}_{\alpha\beta}. \tag{5.17}$$

It will now be shown how ϕ^{ind}_H depends on ϕ^{sc}. We write the induced density as

$$\delta n_s(\mathbf{r}, t) = \delta n_s(\mathbf{r}, \omega)e^{-i\omega t+\eta t} \tag{5.18}$$

and evaluate $\delta n_s(\mathbf{r}, \omega)$;

$$\delta n_s(\mathbf{r}, \omega) = \mathrm{Tr}(\delta(\hat{\mathbf{r}} - \mathbf{r})\delta\rho(\omega)) \tag{5.19}$$

$$= \sum_\gamma \langle\Psi_\gamma|\delta(\hat{\mathbf{r}} - \mathbf{r})\delta\rho(\omega)|\Psi_\gamma\rangle \tag{5.20}$$

$$= \sum_{\delta,\gamma}\int d\mathbf{r}'\langle\Psi_\gamma|\mathbf{r}'\rangle\langle\mathbf{r}'|\delta(\hat{\mathbf{r}} - \mathbf{r})|\Psi_\delta\rangle\langle\Psi_\delta|\delta\rho(\omega)|\Psi_\gamma\rangle \tag{5.21}$$

$$= \sum_{\delta,\gamma}\Psi^*_\gamma(\mathbf{r})\Psi_\delta(\mathbf{r})\delta\rho_{\delta\gamma}(\omega). \tag{5.22}$$

Here, the closure relations

$$\sum_{\delta} |\Psi_\delta\rangle\langle\Psi_\delta| = \mathbf{1},$$
$$\int d\mathbf{r}'|\mathbf{r}'\rangle\langle\mathbf{r}'| = \mathbf{1},$$

were used. By inserting (5.18) and (5.22) into the expression (5.2) for the induced Hartree potential, and writing

$$\phi^{ind}_{H,\alpha\beta}(\mathbf{r},t) = \phi^{ind}_{H,\alpha\beta}(\mathbf{r},\omega)e^{-i\omega t+\eta t},$$

we obtain

$$\phi^{ind}_{H,\alpha\beta}(\omega) = -\frac{1}{e}\sum_{\delta,\gamma} H_{\alpha\beta,\delta\gamma}\delta\rho_{\delta\gamma}(\omega), \tag{5.23}$$

where

$$H_{\alpha\beta,\delta\gamma} := \frac{e^2}{4\pi\epsilon_r\epsilon_0}\int\limits_{\mathbf{R}^2} d\mathbf{r}\Psi^*_\alpha(\mathbf{r})\Big\{\int\limits_{\mathbf{R}^2} d\mathbf{r}'\frac{\Psi^*_\gamma(\mathbf{r}')\Psi_\delta(\mathbf{r}')}{|\mathbf{r}-\mathbf{r}'|}\Big\}\Psi_\beta(\mathbf{r}). \tag{5.24}$$

With use of (5.17), we have

$$\phi^{ind}_{H,\alpha\beta} = \sum_{\delta,\gamma} H_{\alpha\beta,\delta\gamma}f^{\delta\gamma}(\omega)\phi^{sc}_{\delta\gamma}, \tag{5.25}$$

which shows explicitly the dependence of ϕ^{ind}_H on ϕ^{sc}. Equation (5.1) then reads

$$\phi^{sc}_{\alpha\beta} = \phi^{ext}_{\alpha\beta} + \sum_{\delta,\gamma} H_{\alpha\beta,\delta\gamma}f^{\delta\gamma}(\omega)\phi^{sc}_{\delta\gamma} \tag{5.26}$$

or

$$\sum_{\delta,\gamma}\Big\{\delta_{\alpha\delta,\beta\gamma} - H_{\alpha\beta,\delta\gamma}f^{\delta\gamma}(\omega)\Big\}\phi^{sc}_{\delta\gamma} = \phi^{ext}_{\alpha\beta}. \tag{5.27}$$

This relation defines the dielectric tensor. As an analogy to

$$\epsilon\mathbf{E} = \mathbf{D}$$

($\mathbf{E}$ the total electric field and $\mathbf{D}$ the external field), the dielectric tensor elements are defined as [17, 18]

$$\epsilon_{\alpha\beta,\delta\gamma}(\omega) = \delta_{\alpha\delta,\beta\gamma} - H_{\alpha\beta,\delta\gamma}f^{\delta\gamma}(\omega). \tag{5.28}$$

For a given ϕ^{ext}, we can calculate ϕ^{sc} via ϵ^{-1}. For a weak external perturbation, the general excitation spectrum can be found by determining the roots of

$$\det\epsilon(\omega) = 0.$$

5.2 Power absorption

The equation for the power absorption is given with

$$\mathcal{P}(\omega) = \frac{1}{2}\Re \int \Big\{ \delta\mathbf{J}(\mathbf{r},\omega) \cdot (\mathbf{E}^{sc}(\mathbf{r},\omega))^* \Big\} \mathbf{dr}, \tag{5.29}$$

where $\mathbf{E}^{sc}$ is the self-consistent field; it is the **total** electric field experienced by the electrons. This is the Joule heating of the system. The equation has already been Fourier transformed with respect to time, using the definition (5.9). $\delta\mathbf{J}(\mathbf{r},\omega)$ is the induced current caused by the external disturbance ϕ^{sc}. The total electric field $\mathbf{E}^{sc}$ is simply the negative gradient of the self-consistent potential:

$$\mathbf{E}^{sc} = -\nabla\phi^{sc}. \tag{5.30}$$

By using the following identity from vector calculus

$$\nabla \cdot ((\phi^{sc})^* \delta\mathbf{J}) = \nabla(\phi^{sc})^* \cdot \delta\mathbf{J} + (\phi^{sc})^* (\nabla \cdot \delta\mathbf{J}) \tag{5.31}$$

and equation (5.30), the integral in equation (5.29) can be written as

$$\begin{aligned} -\int \delta J(\mathbf{r},\omega) \cdot \nabla(\phi^{sc}(\mathbf{r},\omega))^* \mathbf{dr} = &\int (\phi^{sc}(\mathbf{r},\omega))^* (\nabla \cdot \delta\mathbf{J}(\mathbf{r},\omega)) \mathbf{dr} \\ &- \int \nabla \cdot ((\phi^{sc}(\mathbf{r},\omega))^* \delta\mathbf{J}(\mathbf{r},\omega)) \mathbf{dr}. \end{aligned} \tag{5.32}$$

One can now choose

$$\delta\mathbf{J}(\mathbf{r},\omega) = 0 \qquad \text{for} \quad r \geq R, \tag{5.33}$$

where R can be extended into the region far from the dot, where the wavefunctions are negligible. This is possible since the quantum dot system we are investigating is a limited system in size. Let A be the area which satisfies $r \leq R$. By Gauss's theorem, the last integral in (5.32) is

$$\int \nabla \cdot ((\phi^{sc}(\mathbf{r},\omega))^* \delta\mathbf{J}(\mathbf{r},\omega)) \mathbf{dr} = \int_{\delta A} ((\phi^{sc}(\mathbf{r},\omega))^* \delta\mathbf{J}(\mathbf{r},\omega)) \cdot d\ell \tag{5.34}$$

and is therefore equal to zero according to condition (5.33). We thus have

$$\int_{\mathbf{R}^2} \delta J(\mathbf{r},\omega) \cdot \nabla(\phi^{sc}(\mathbf{r},\omega))^* \mathbf{dr} = -\int_{\mathbf{R}^2} (\phi^{sc}(\mathbf{r},\omega))^* (\nabla \cdot \delta\mathbf{J}(\mathbf{r},\omega)) \mathbf{dr}. \tag{5.35}$$

Equation (5.29) can now be rewritten as

$$\mathcal{P}(\omega) = \frac{1}{2}\Re \Big\{ \int (\phi^{sc}(\mathbf{r},\omega))^* (\nabla \cdot \delta\mathbf{J}(\mathbf{r},\omega)) \mathbf{dr} \Big\}. \tag{5.36}$$

We now wish to express $\nabla \cdot \delta\mathbf{J}$ in terms of the induced density through the equation of continuity

$$-e\frac{\partial(\delta n_s)}{\partial t}(\mathbf{r},t) + \nabla \cdot \delta\mathbf{J}(\mathbf{r},t) = 0, \tag{5.37}$$

where $\delta n_s(\mathbf{r},t)$ is the induced electron density. The equation of continuity only includes the induced density, since it is the only part of the density depending on time. In $(\mathbf{r},\omega)$ space, it reads

$$ie\omega\delta n_s(\mathbf{r},\omega) + \nabla \cdot \delta\mathbf{J}(\mathbf{r},\omega) = 0. \tag{5.38}$$

The power absorption thus becomes

$$\mathcal{P}(\omega) = \frac{e\omega}{2}\Im\Big\{\int (\phi^{sc}(\mathbf{r},\omega))^*\delta n_s(\mathbf{r},\omega)\mathbf{dr}\Big\}, \tag{5.39}$$

where we have used the property

$$\Re(iz) = -\Im(z) \qquad \text{for} \quad z \in \mathbf{C}.$$

The integral in eq. (5.39) can be expressed as

$$\int (\phi^{sc}(\mathbf{r},\omega))^*\delta n_s(\mathbf{r},\omega)\mathbf{dr} = \int \mathbf{dr} \sum_{\alpha,\beta} \Psi^*_\alpha(\mathbf{r})(\phi^{sc}(\mathbf{r},\omega))^*\Psi_\beta(\mathbf{r})(-ef^{\beta\alpha}(\omega))\phi^{sc}_{\beta\alpha} \tag{5.40}$$

$$= \sum_{\alpha,\beta}(-ef^{\beta\alpha}(\omega))(\phi^{sc*}_{\alpha\beta})\phi^{sc}_{\beta\alpha}, \tag{5.41}$$

with help of eq. (5.22) and (5.17). This leads to

$$\mathcal{P}(\omega) = \frac{-e^2\omega}{2}\Im\Big\{\sum_{\alpha,\beta} f^{\beta\alpha}(\omega)\Big|\phi^{sc}_{\beta\alpha}\Big|^2\Big\}, \tag{5.42}$$

where the identity

$$(\phi^{sc*}_{\alpha\beta}) = (\phi^{sc}_{\beta\alpha})^*$$

has been used. Eq. (5.42) shows explicitly that when $\eta = 0$, there is no power absorption, simply by writing $f^{\beta\alpha}(\omega)$ (defined in eq. (5.16)) as a real and imaginary part. When no damping is involved, described here by η, no power is lost in the system. Equation (5.42) is sometimes seen in the form

$$\mathcal{P}(\omega) = \frac{-e^2\omega}{2}\Im\Big\{\sum_{\alpha,\beta} f^{\beta\alpha}(\omega)(\phi^{ext}_{\beta\alpha})^*\phi^{sc}_{\beta\alpha}\Big\} \tag{5.43}$$

as if $\mathbf{E}^{sc}$ had been replaced with $\mathbf{E}^{ext}$. To show this, we will start with the expression

$$\mathbf{E}^{sc} = \mathbf{E}^{ext} - \frac{i}{\epsilon_0 \epsilon_r \omega} \delta \mathbf{J} \tag{5.44}$$

and show that it is consistent, with the aid of the equation of continuity, with Poisson's equation. We rewrite (5.44) using eq. (5.30)

$$\nabla \phi^{sc} = \nabla \phi^{ext} + \frac{i}{\epsilon_0 \epsilon_r \omega} \delta \mathbf{J}, \tag{5.45}$$

or

$$\nabla \phi^{ind} = \frac{i}{\epsilon_0 \epsilon_r \omega} \delta \mathbf{J}, \tag{5.46}$$

where eq. (5.1) has been used. We now apply ∇ and obtain

$$\nabla \cdot (\nabla \phi^{ind}) = \frac{i}{\epsilon_0 \epsilon_r \omega} \nabla \cdot (\delta \mathbf{J}) \tag{5.47}$$

$$= \frac{i}{\epsilon_0 \epsilon_r \omega} (-ie\omega) \delta n_s \qquad \text{(eq. of continuity (5.38))} \tag{5.48}$$

$$= \frac{e}{\epsilon_0 \epsilon_r} \delta n_s. \tag{5.49}$$

The last one is precisely Poisson's equation. In addition, equation (5.44), or equivalently eq. (5.46), is the only solution to Poisson's equation if one requires that $\mathbf{E^{ind}} = 0$ and $\delta \mathbf{J} = 0$ at $r = +\infty$.
We now have in equation (5.29)

$$\mathcal{P}(\omega) = \frac{1}{2} \Re \int \left\{ \delta \mathbf{J}(\mathbf{r}, \omega) \cdot (\mathbf{E}^{sc}(\mathbf{r}, \omega))^* \right\} \mathbf{dr} \tag{5.50}$$

$$= \frac{1}{2} \Re \int \left\{ \delta \mathbf{J}(\mathbf{r}, \omega) \cdot \left(\mathbf{E}^{ext}(\mathbf{r}, \omega) - \frac{i}{\epsilon_0 \epsilon_r \omega} \delta \mathbf{J}(\mathbf{r}, \omega) \right)^* \right\} \mathbf{dr} \tag{5.51}$$

$$= \frac{1}{2} \Re \int \left\{ \delta \mathbf{J}(\mathbf{r}, \omega) \cdot (\mathbf{E}^{ext}(\mathbf{r}, \omega))^* \right\} \mathbf{dr} \tag{5.52}$$

and this leads precisely to equation (5.43).

To simulate the far-infrared response of the quantum dot, the power absorption, from eq. (5.42), is calculated with the external potential

$$\phi^{ext}(\mathbf{r}, t) = \phi_0 r e^{i(N_p \phi - \omega t)}, \qquad \text{where} \quad N_p = \pm 1$$

and ϕ_0 can be assumed to be real and constant. The external electric field is then spatially constant,

$$\mathbf{E}^{ext} = -\phi_0 (\hat{\mathbf{e}}_x + i N_p \hat{\mathbf{e}}_y) e^{-i\omega t}, \tag{5.53}$$

and $E_y = i N_p E_x$. For $N_p = +1$, $\mathbf{E}^{ext}$ represents a right circularly polarized wave (clockwise rotation of $\Re(\mathbf{E}^{ext})$ in the (x, y)-plane). If $N_p = -1$ we have a left circular polarization (counterclockwise rotation of $\Re(\mathbf{E}^{ext})$ in the (x, y)-plane) [19].

Chapter 6

Absorption of harmonic quantum dots

6.1 Selection rules

For a strictly circular symmetric harmonic dot, the dipole selection rule for the center-of-mass angular momentum is $\Delta M = -N_p$. For left circular polarization, there is only absorption into ω_- and for right circular polarization, only into ω_+ (eq. (2.6)) [3]. For an anisotropic harmonic confinement, the selection rule is still $\Delta M = \pm 1$, but there is absorption into both ω_+ and ω_- for each polarization. The resonance frequencies are then given by (see eq. (2.8))

$$\omega_\pm^2 = \frac{\omega_x^2 + \omega_y^2 + \omega_c^2 \pm [\omega_c^4 + 2\omega_c^2(\omega_x^2 + \omega_y^2) + (\omega_x^2 - \omega_y^2)^2]^{1/2}}{2}. \tag{6.1}$$

where ω_x and ω_y are the resonances at $B = 0$ T. In particular, the intensity ratios of absorption can be obtained [2]

$$\frac{f_-}{f_+} = g_b^2 \frac{\omega_-}{\omega_+} \frac{2\omega_+ - \omega_c}{2\omega_- + \omega_c} \quad \text{for} \quad N_p = +1 \quad (E_y = +iE_x), \tag{6.2}$$

where

$$g_b = \frac{\omega_x^2 - \omega_y^2}{2\left(\omega_-^2 - \omega_c\omega_- - \frac{\omega_x^2+\omega_y^2}{2}\right)},$$

and

$$\frac{f_+}{f_-} = g_a^2 \frac{\omega_+}{\omega_-} \frac{2\omega_- + \omega_c}{2\omega_+ - \omega_c} \quad \text{for} \quad N_p = -1 \quad (E_y = -iE_x), \tag{6.3}$$

where

$$g_a = \frac{\omega_x^2 - \omega_y^2}{2\left(\omega_+^2 + \omega_c\omega_+ - \frac{\omega_x^2+\omega_y^2}{2}\right)}.$$

For an isotropic harmonic confinement, $\omega_x = \omega_y$ and thus $g_a = 0 = g_b$ as expected.

The absorption was calculated with a small finite constant value of η ($= 0.05\hbar\omega_0$, where $\hbar\omega_0 = 3.37$ meV). A finite value of η produces finite linewidths of absorption peaks (a phenomenological Lorentzian line broadening).

6.2 Circular parabolic dots

The excitation spectrum of a two electron circular parabolic dot was calculated. The results are shown in Figure 6.1. The generalized Kohn theorem was never used explicitly and mixing of all angular quantum numbers, M, within the truncated basis chosen, was allowed. Even so, Kohn's theorem is fulfilled and the resonance frequencies are in accordance with the theoretical equation (2.6).

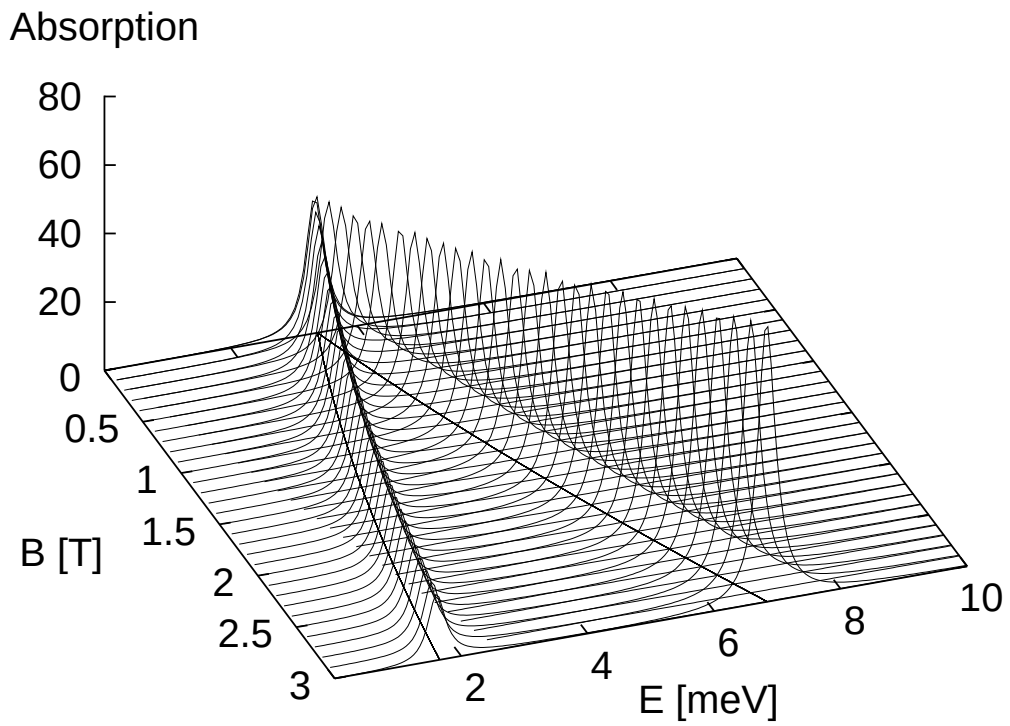

Figure 6.1: The power absorption of a two electron circular parabolic dot for $N_p = +1$ (upper branch) and $N_p = -1$ (lower branch). The resonance frequencies are fitted to eq. (2.6). Kohn's theorem is fulfilled.

6.3 Elliptic dots

Model calculations of power absorption

The power absorption of two electron elliptic quantum dots was found for both right and left circular polarization of the incident wave. The results are shown in Figures 6.2 ($\alpha_1 = 0.2$) and 6.5 ($\alpha_1 = 0.4$). For a given external magnetic field, two peaks appear for each polarization. This truly agrees with the generalized Kohn theorem for elliptic quantum dots (section 2.3). The two branches are plotted in the figures, according to eq. (6.1). The intensities of absorption for the resonance peaks were found from the data in Figs. 6.2 and 6.5. Figures 6.3 and 6.4 show the intensity ratios found from the data, compared with equations (6.2) and (6.3) where $\omega_\pm$ are found with equation (6.1). The data fits well to the theoretical curves. The model used in the calculations, as discussed earlier (section 3.2.3), allows for mixing of all angular momentum quantum numbers, M. As in section 6.2, the generalized Kohn theorem has never been used explicitly but the results of the model calculations, both for the resonance frequencies and the intensity ratios, show that it is fulfilled.

Other model calculations

Few model calculations have been made on elliptic quantum dots. In addition to a proof of Kohn's theorem for anisotropic harmonic quantum dots [2, 13], mostly ground state calculations have been performed. Ezaki *et al.* evaluated in [20] the addition energy of circular, elliptic, and triangular quantum dots at zero magnetic field. They diagonalized the N-electron Hamiltonian in a truncated basis, with the Coulomb interaction for $N = 2 - 12$, obtaining clear peaks in the addition energy spectrum of circular and triangular dots, where the dots have a complete shell filling structure, but for elliptic dots the peak structure is lot less clear. They explained it to be the result of a splitting of the degenerate eigenstates, and also due to mixing of various eigenstates with different angular momenta.

Madhav and Chakraborty calculated analytically the energy levels of a single-electron elliptic quantum dot [21]. Qualitatively, the energy spectrum is similar to what is found here. They calculated the energy levels of a two electron circular parabolic quantum dot by assuming an inter-particle potential of non-Coulombic form $V(r) \propto 1/r^2$. Most of the analysis can then be performed analytically. The energy levels of a two electron elliptic quantum dot were found by perturbation calculations, assuming that the anisotropy is small.

Far-infrared measurements on elliptic quantum dots

Claus Dahl measured absorption of many electron elliptic dots with a major axis $w_x = 116$ μm and a minor axis $w_y = 40$ μm [22]. They are relatively large such that the resonance frequencies lie in the sub-millimetric range. The measurements

were in accordance with the expected behavior of elliptic dots and the predictions of Kohn's theorem.

Elisabeth Vasiliadou reported FIR measurements in [23] on elliptic dots with $w_x = 320$ nm and $w_y = 85$ nm and fixed gate voltage $V_g = -0.3$ V (fixed electron number). An anticrossing occurs in the vicinity of $B = 1$ T, reminiscent of a square symmetric confinement discussed in the next chapter. Resonance frequencies at $B = 0$ T and 4 T were measured as a function of electron number ($V_g \in [-0.4; 0.0]$ V) and unpolarized incident light.

Markus Hochgräfe reported in his diploma thesis [5] FIR measurements on an array of elliptic dots. The dots had a major axis $w_x = 600$ nm and a minor axis $w_y = 400$ nm and measurements were performed with 8, 48 and 82 electrons per dot. For 8 electrons per dot, the results fit to the expected resonance frequencies of an elliptic dot and Kohn's theorem holds. However, for 48 electrons per dot, one anticrossing occurs and several for 82 electrons per dot. Probably, the confinement potential is no longer parabolic, due to screening.

Bernstein modes were also observed [7, 24]. They appear as an interaction, at or near the crossing of a dot (or quantum wire) modes with harmonics of the cyclotron frequency; $2\omega_c$, $3\omega_c$, ... For 48 electrons in a dot, an interaction with $2\omega_c$ occurs, and with $2\omega_c$ and $3\omega_c$ for 82 electrons.

In this chapter, we have seen that the calculations are in agreement with the predictions of the generalized Kohn theorem. The FIR radiation couples only to the center-of-mass motion of the electron system. For quantum dots subject to a square symmetric confinement potential, the theorem no longer applies. In the following chapter, absorption of such quantum dots will be investigated and evidence of the interaction in the absorption will be discussed.

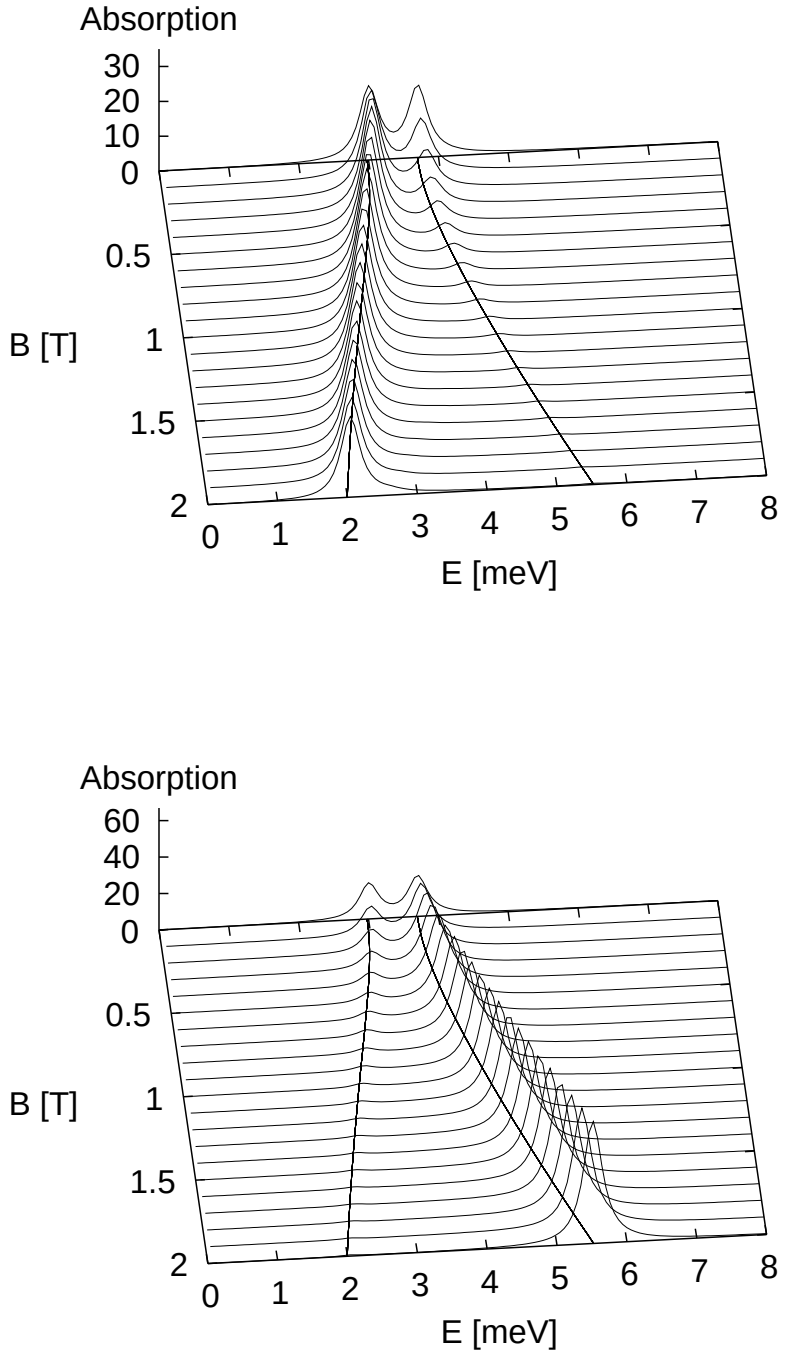

Figure 6.2: The excitation spectrum for $N_p = -1$ (above) and $N_p = +1$ (below). The resonance positions are plotted according to eq. (6.1) with $\hbar\omega_x = 3.70$ meV and $\hbar\omega_y = 2.98$ meV. $\alpha_1 = 0.2$.

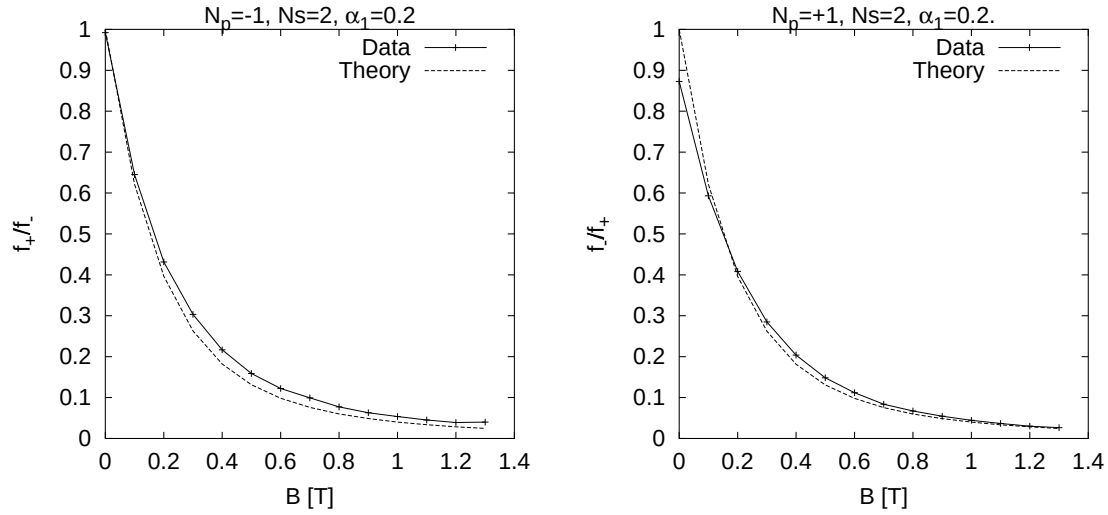

Figure 6.3: The ratios of intensity of absorption for both polarizations as a function of the magnetic field. The deviation coefficient is $\alpha_1 = 0.2$. The theoretical curves are plotted with $\hbar\omega_x = 3.70$ meV and $\hbar\omega_y = 2.98$ meV, the energy resonances at $B = 0$ T.

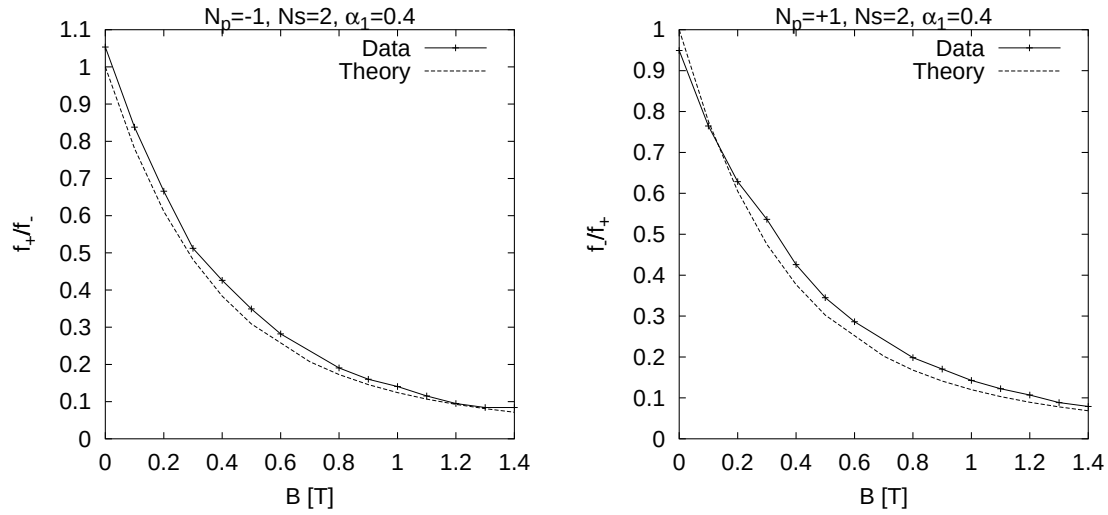

Figure 6.4: The ratios of intensity of absorption for $N_p = \pm 1$ and $\alpha_1 = 0.4$ as a function of the magnetic field. The theoretical curves are plotted with $\hbar\omega_x = 4.13$ meV and $\hbar\omega_y = 2.75$ meV, the energy resonances at $B = 0$ T.

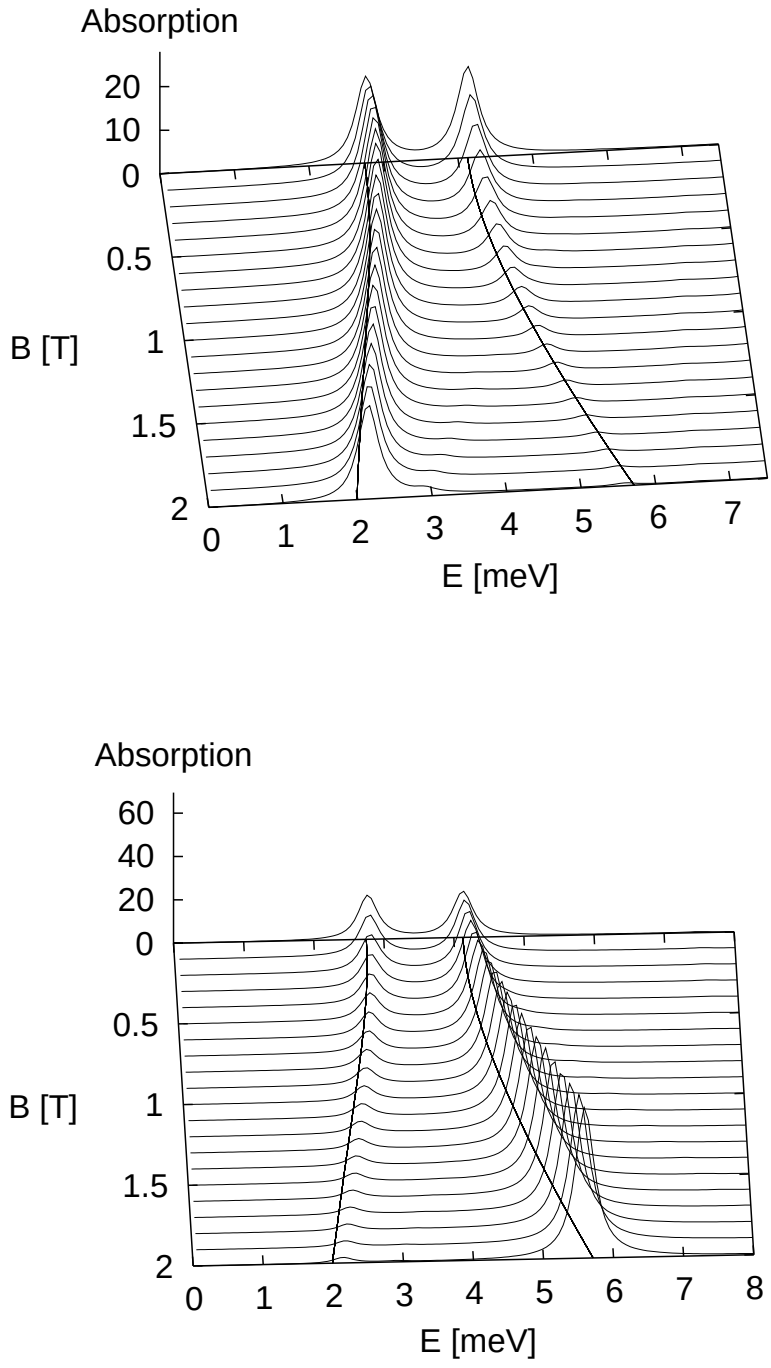

Figure 6.5: The excitation spectrum for $N_p = -1$ (above) and $N_p = +1$ (below). The resonance positions are plotted according to eq. (6.1) with $\hbar\omega_x = 4.13$ meV and $\hbar\omega_y = 2.75$ meV. $\alpha_1 = 0.4$.

Chapter 7

Absorption of quantum dots with square symmetry

For quantum dots subject to a square symmetric confinement potential, we are out of the range of the generalized Kohn theorem and it should be possible to observe evidence of the interaction in the absorption spectrum. We will focus our attention here on the absorption of two electrons. The evolution of absorption peaks at $B = 0$ T, as α_2 is increased, will be shown. The induced density for a pronounced square symmetric confinement ($\alpha_2 = 0.40$) at $B = 0$ T is used to identify the relative motion of the electrons. Excitation spectra for $\alpha_2 = 0.20$ and 0.40 will be discussed.

7.1 The power absorption and the induced density at zero magnetic field

The power absorption at $B = 0$ T for increasing square symmetric deviation from the circular parabolic confinement is shown in Fig. 7.1. For small α_2 (< 0.1) the far-infrared radiation couples only to the center-of-mass motion and one absorption peak occurs, as in the isotropic harmonic confinement. For larger α_2, the square symmetric confinement starts to show up in the absorption spectrum. A new peak occurs for $\alpha_2 = 0.10$ which increases in oscillator strength with increasing α_2, whereas the "center-of-mass" peak decreases at the same time. They have almost equal strength for $\alpha_2 = 0.40$. To understand better the behavior of the electron system at $B = 0$ T, when exposed to the FIR radiation, it can be useful to look at the induced density. We write it to be

$$\delta n_s(\mathbf{r}, t) = \delta n_s(\mathbf{r}, \omega) e^{-i\omega t + \eta t} \tag{7.1}$$

as in eq. (5.18), where

$$\delta n_s(\mathbf{r}, \omega) = \sum_{\delta,\gamma} \Psi^*_\gamma(\mathbf{r}) \Psi_\delta(\mathbf{r}) \delta\rho_{\delta\gamma}(\omega). \tag{7.2}$$

By convention from electromagnetic theory, the induced density is evaluated as $\Re(\delta n_s(\mathbf{r}, t))$. We choose $t = 0$. The induced density at the absorption peaks for a strong square symmetric confinement ($\alpha_2 = 0.40$) is shown in Figure 7.2 for $N_p = -1$. A simple dipole is induced at $E = 2.38$ meV, reflecting an almost pure center-of-mass motion. The absorption peak is however weak in oscillator strength. The motion induced is the lowest mode of oscillation of odd parity. Modes of even parity are not excited, due to the parity of the external potential. The next lowest mode of oscillation is induced at 3.15 meV, showing the relative motion of the electrons. The motion induced at 3.99 meV seems to be of a rather circular kind.

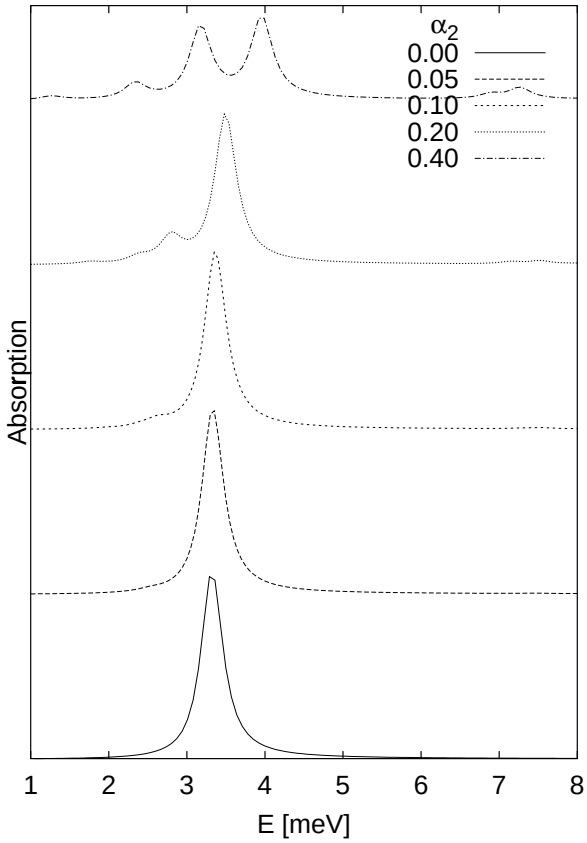

Figure 7.1: Evolution of absorption peaks at $B = 0$ T as α_2 is increased for left circular polarization ($N_p = -1$). For $\alpha_2 = 0.05$, one peak occurs, as in the circular parabolic confinement (coupling of the FIR to center-of-mass motion). For $\alpha_2 \geq 0.1$, the effect of the square deviation becomes evident. An extra peak occurs which increases with increasing α_2. At the same time, the oscillator strength of the "center-of-mass peak" decreases.

7.2 Excitation spectra

The power absorption was calculated as a function of energy of the incident wave ($E = \hbar\omega$) and magnetic field (B) for $\alpha_2 = 0.20$ (Fig. 7.5) and $\alpha_2 = 0.40$ (Fig. 7.6). The corresponding frequency dispersions (position of resonance peaks as a function of B) for both polarizations are shown in Figure 7.7.

To see whether there are transitions for which the incident light couples only to the center-of-mass motion, one must look at the *non-interacting* Darwin-Fock (DF) spectrum. The energy for which such transitions occur will then coincide with an energy difference of an energy level of the non-interacting spectrum and its lowest level for a given B. For $\alpha_2 = 0.20$, this comparison of the DF spectrum and the frequency dispersion (resonance frequencies as a function of B), showed that the lower branch for $N_p = -1$ converges asymptotically to a "center-of-mass transition". For $N_p = +1$, the lower branch for $B \approx 0.1 - 0.3$ T seems to exhibit center-of-mass behavior.

The higher branch for $N_p = -1$ and $\alpha_2 = 0.20$ decreases rapidly in oscillator strength as B increases and vanishes at approximatively 1.0 T. It can be identified as a one electron transition with many-body effects, by comparison to the *interacting* DF spectrum. It corresponds to the energy difference of an energy level and the next lowest level, There are two electrons in the dot, such that the two lowest levels are occupied. However, the transition occurs at a higher energy by ≈ 0.7 meV than the energy difference of the DF spectrum predicts. This is the so-called *depolarization shift*. It originates in the fact that when one electron is moved, the other electrons move also, due to the Coulomb interaction. This many-particle behavior requires a somewhat higher energy for absorption to occur.

Another such transition, low in oscillator strength, occurs in the higher branch for $N_p = +1$ when $B \approx 0.4 - 0.8$ T. It is seen in the interacting DF spectrum as the energy difference (with a depolarization shift) of one energy level and the lowest one.

If we consider now the stronger square deviation from the isotropic harmonic confinement, $\alpha_2 = 0.40$, some coupling to the center-of-mass motion is still seen. The lowest branch for $N_p = -1$ converges asymptotically to a "center-of-mass resonance" with increasing B, as in the case of $\alpha_2 = 0.20$. Also, the middle branch for $N_p = +1$ is a center-of-mass resonance in the range 0.5-1.9 T. A somewhat similar behavior was seen for $\alpha_2 = 0.20$ but it was "disturbed" sooner by the anticrossing, discussed later in this section. The lowest branch for $N_p = +1$, weak in oscillator strength, is a one electron transition for B=0.3-0.8 T, with a depolarization shift of approximatively 0.7 meV.

Anticrossing behavior shows in the excitation spectra for both $\alpha_2 = 0.20$ and 0.20 and right circular polarization ($N_p = +1$). Its origin shows already in the

single electron energy spectrum, leaving its trace in the interacting spectrum. The square symmetric term of the deviation confinement, $\cos(4\phi)$, couples the states $(M, n_r) = (+1, 0)$ and $(-3, 0)$ (see section 3.2.2). Those are accidentally degenerate for the isotropic harmonic confinement, at $B \approx 2.3$ T in the non-interacting case, but the coupling lifts the degeneracy. This leads to the anticrossing at this magnetic field (see the left figures in Figs. 7.3 and 7.4). For two interacting electrons, anticrossing also appears but shifted to a lower magnetic field. Figures 7.3 and 7.4 show this anticrossing behavior at $B \approx 1.4$ T; shifting to lower magnetic fields due to the Coulomb interaction has already been pointed out in [25].

For the stronger square symmetric deviation, $\alpha_2 = 0.40$ (Fig. 7.6), the highest branch can be traced as a one electron transition with a depolarization shift of approximatively 0.7 meV, whereas for the weaker deviation, $\alpha_2 = 0.20$, the excitation has the characteristics of a center-of-mass motion with however some many-body effects.

7.2.1 Observation of anticrossing in other model calculations and experiments

Effects on excitation spectra of a square symmetric deviation from a parabolic confinement potential were found in [25] by D. Pfannkuche and R. R. Gerhardts. They performed exact calculations on a two electron quantum dot, where the deviation confinement was taken to be of the form

$$U(\mathbf{r}) = \frac{1}{2} m^* \omega_4^2 (ar^4 + bx^2y^2),$$

i. e. both a circular symmetric and square symmetric term. An anticrossing behavior was found for $a = 1$ Å$^{-2} = b$ whereas no anticrossing occurred for $a = 1$ Å^{-2} and $b = 0$. It is thus due to the x^2y^2 confinement term.

Anticrossing has also been observed experimentally for square quantum dots, by Demel *et al.* [8] for 25 and 210 electrons per dot. The anticrossing effect is seen, even in quantum dots with a weak square symmetric confinement, as is the case in these calculations and experiments.

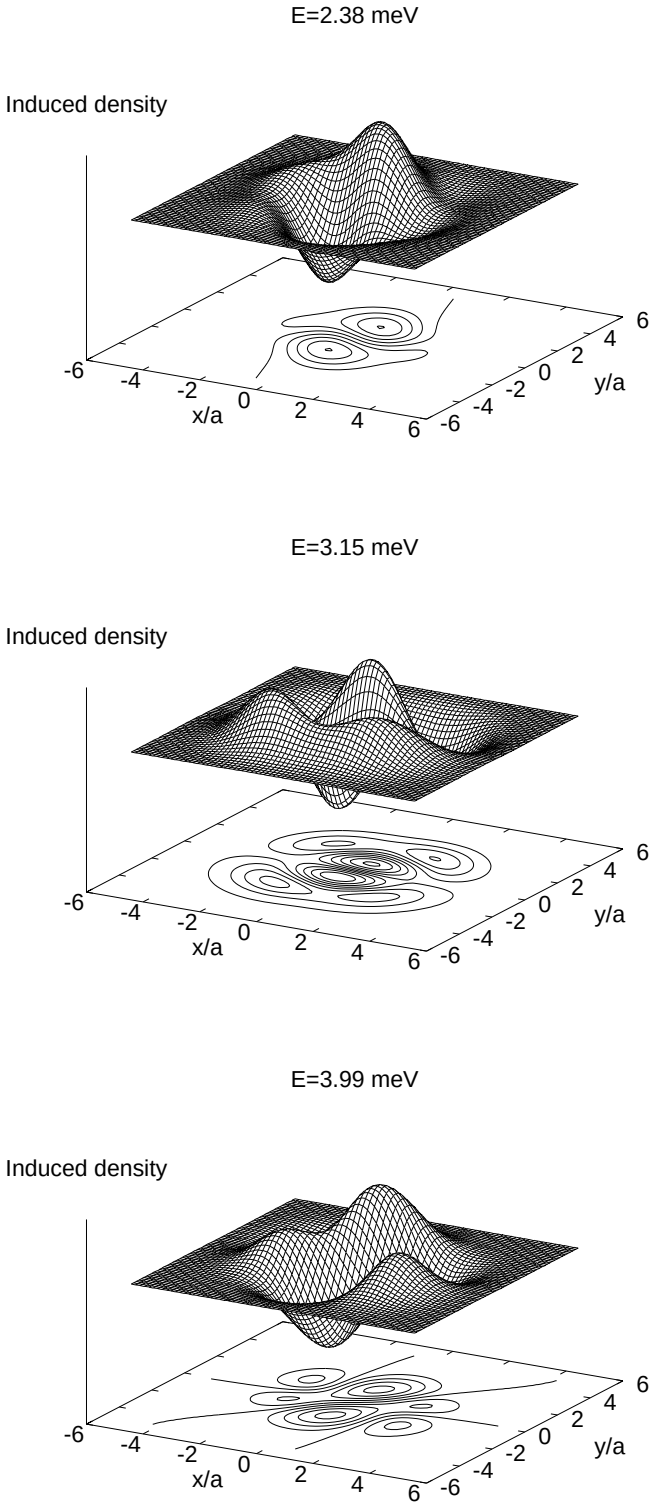

Figure 7.2: The induced density at the absorption peaks for $N_p = -1$. See discussion in text.

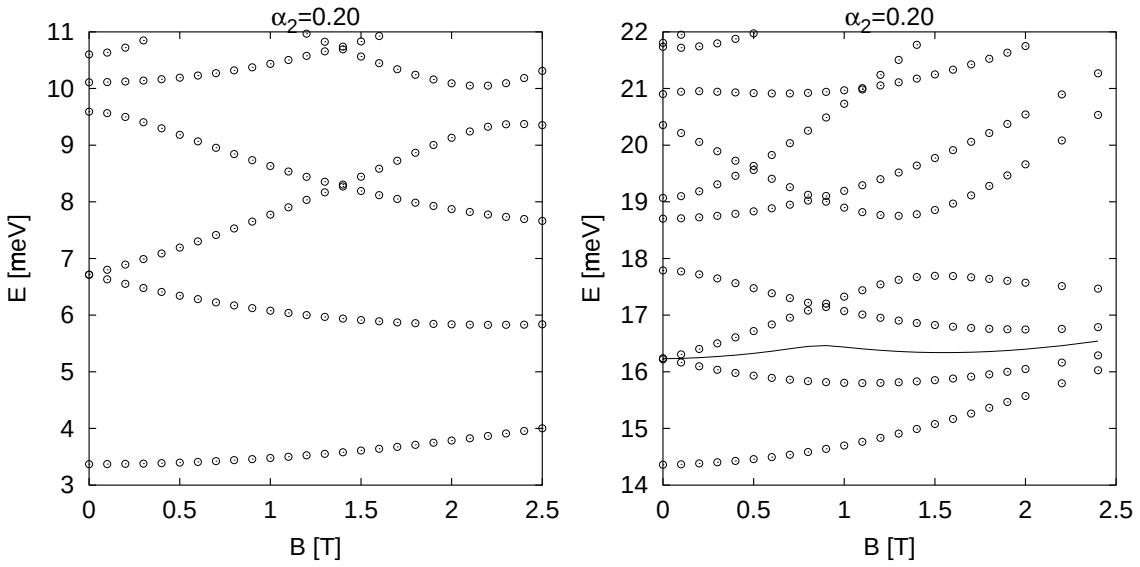

Figure 7.3: Darwin-Fock spectra for $\alpha_2 = 0.20$, non-interacting (left) and two interacting electrons (right). Anticrossing occurs at $B = 2.3$ T in the non-interacting spectrum and around $B = 1.4$ T for the interacting electrons. The chemical potential is given by the solid line.

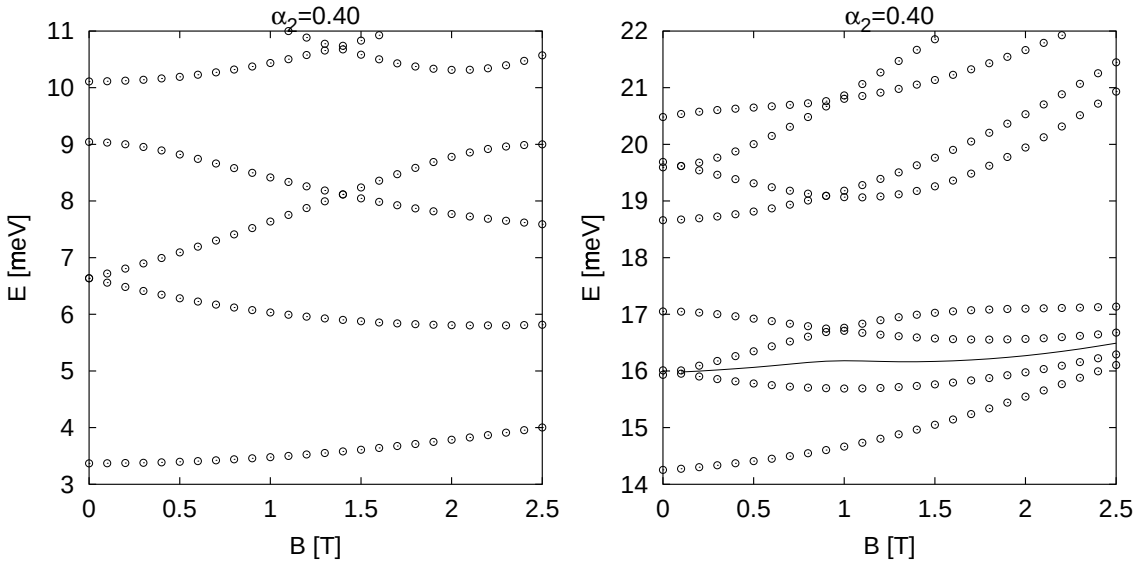

Figure 7.4: Darwin-Fock spectra for $\alpha_2 = 0.40$, non-interacting (left) and two interacting electrons (right). Anticrossing occurs at $B = 2.3$ T in the non-interacting spectrum and in the vicinity of $B = 1.4$ T for the interacting electrons. The chemical potential is given by the solid line.

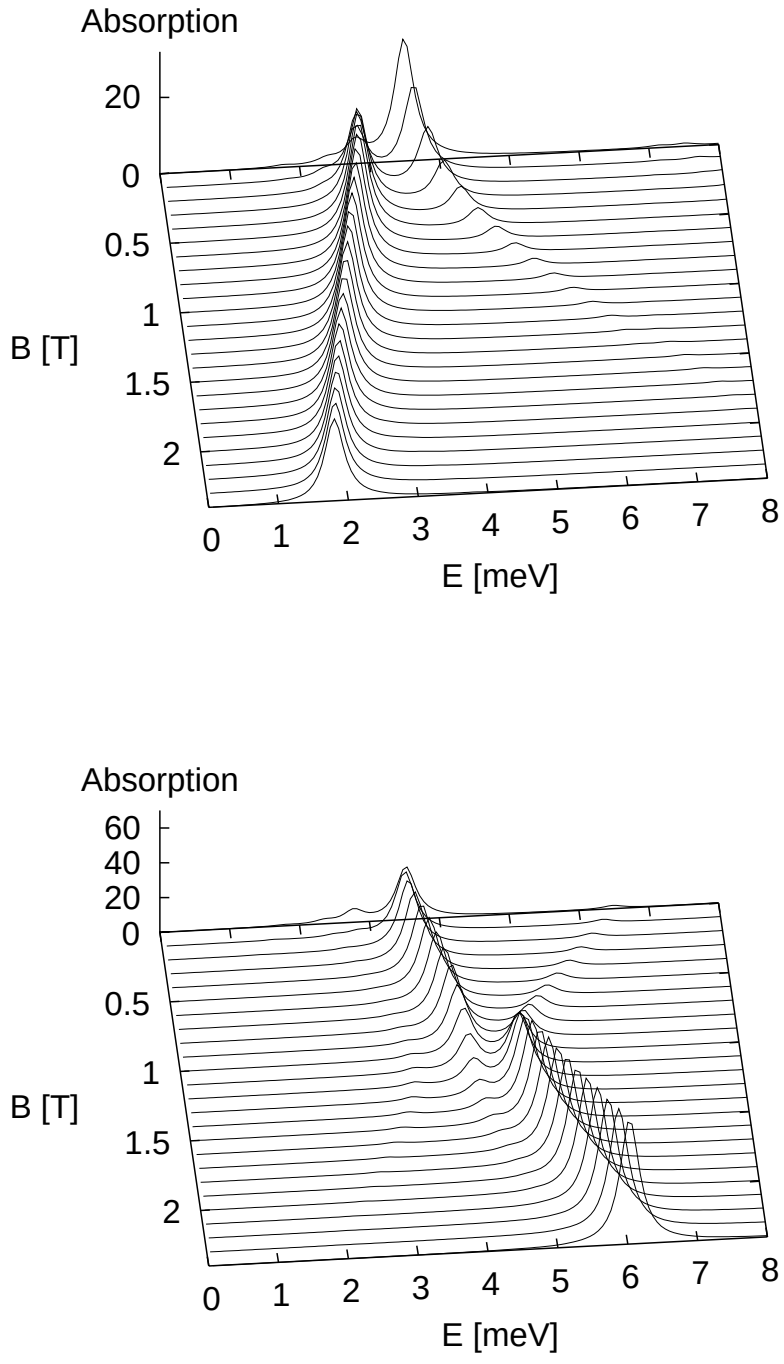

Figure 7.5: The power absorption for $\alpha_2 = 0.20$ as a function of energy of the incident wave ($E = \hbar\omega$) and the magnetic field B. The absorption for left circular polarization, $N_p = -1$, is shown in the upper figure and right circular polarization, $N_p = +1$, in the lower one.

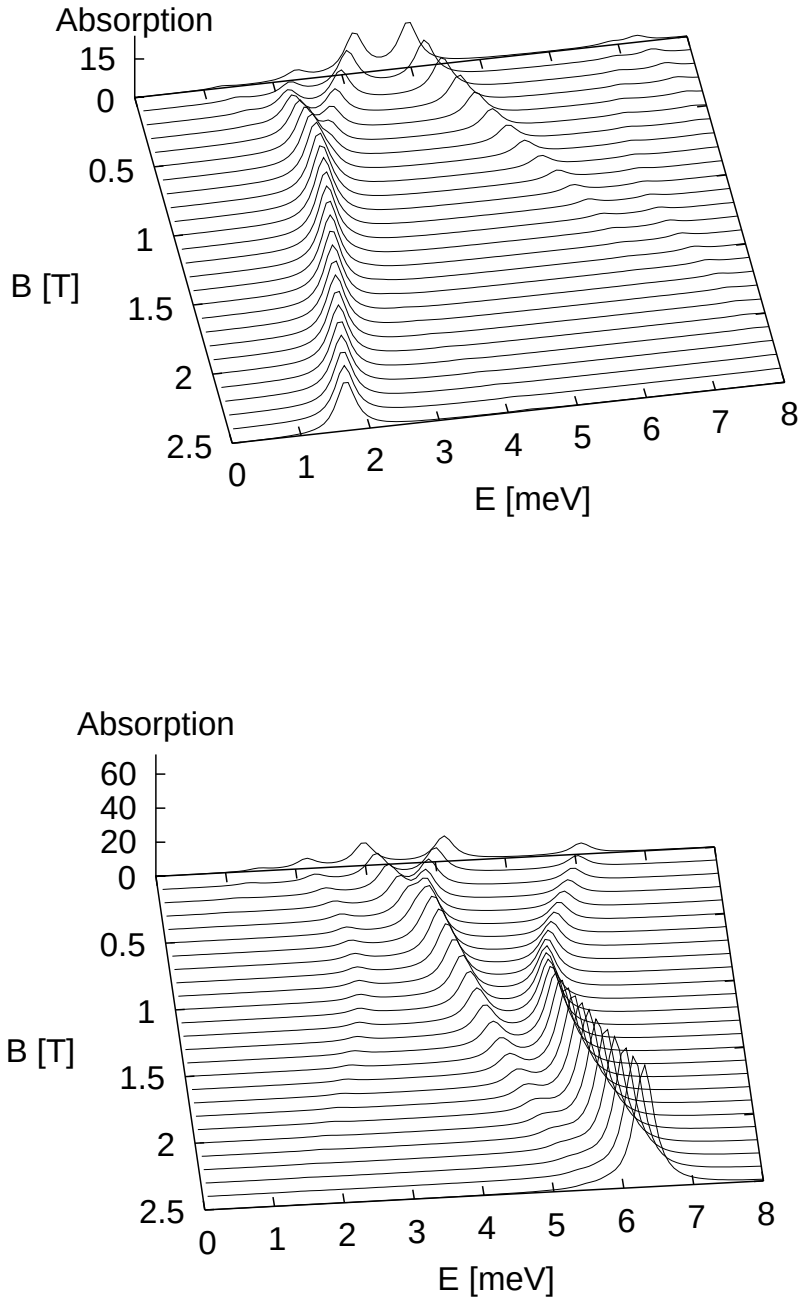

Figure 7.6: The power absorption for $\alpha_2 = 0.40$ as a function of energy of the incident wave, $E = \hbar\omega$, and the magnetic field B. The absorption for left circular polarization, $N_p = -1$, is shown in the upper figure and right circular polarization, $N_p = +1$, in the lower one.

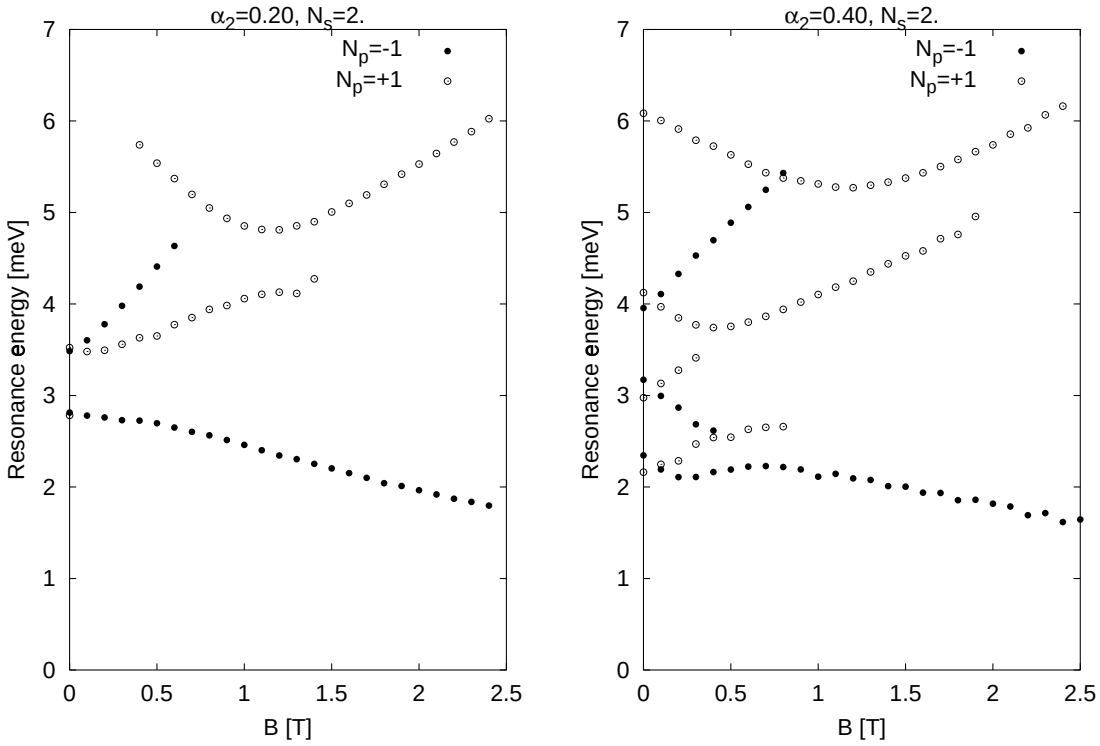

Figure 7.7: The positions of resonance peaks for the excitation spectra in Figures 7.5 ($\alpha_2 = 0.20$) and 7.6 ($\alpha_2 = 0.40$). Both polarizations are shown.

Chapter 8

Conclusions and summary

In this work, the absorption spectra of interacting electrons in a quantum dot, described by circular parabolic, elliptic or square symmetric confinement potentials, in a magnetic field perpendicular to the 2DEG, have been calculated. The attention has been focused on two interacting electrons.

The confinement potential was written as a circular parabolic potential, suitable to model circular quantum dots, and a multipole expansion in two dimensions, with high symmetry, modelling elliptic, square symmetric, hexagonal, ... quantum dots. The multipole expansion of the confinement breaks the circular symmetry which means that the angular momentum is no longer conserved. The model calculations, performed in the basis of eigenfunctions of the circular parabolic potential, thus required mixing of all angular momentum quantum numbers, M. The matrix elements of the confinement potential, and the Hartree potential for the interaction, were evaluated analytically. The maximum values of M and n_r had to be chosen carefully in order to minimize CPU time and maximize the precision.

To emphasize the difference between the circular parabolic confinement and a confinement that breaks the circular symmetry, it should be noted that the Coulomb interaction does *not* mix M in the circular parabolic case, whereas it mixes M even further in the latter case, such as to "recover" in a sense the circular symmetry, i. e. screening effects.

From the calculations, we have seen that the generalized Kohn theorem is fulfilled for a harmonic confinement potential, both circular symmetric and elliptic, and the FIR radiation excites only the center-of-mass motion of the system. Kohn's theorem was never assumed to be valid, and yet, the calculations show that it is fulfilled. However, for the square symmetric confinement potential, the interaction is involved in the absorption and relative motion of the electrons is induced. Kohn's theorem is no longer fulfilled. The induced density at $B = 0$ T revealed relative motion of the electrons. Also, the resonance frequencies of the absorption did not correspond to the energy differences of the single electron energy levels and the lowest level, except for isolated cases. Such correspondence for all the transitions would

show that the only motion induced is a center-of-mass motion. The absorption spectrum includes, in addition to some "center-of-mass transitions", several absorption lines which could be identified from the energy spectrum of interacting electrons as one electron transitions with a depolarization shift, which shows clearly their many-electron character, i. e. interaction effects.

Geometrical effects, identified here in the absorption spectra, such as the anti-crossing phenomenon in the square symmetric confinement potential and the splitting of absorption lines at $B = 0$ T for elliptic dots, have been observed in experiments. A splitting at $B = 0$ T for a strong square confinement, as found here, has however never been observed.

The model described in this thesis is quite general and yet it allows for several extensions. The ground state calculations (i. e. before the infrared light is exposed to the system) could be improved by including the exchange part of the Coulomb interaction via the Hartree-Fock approximation, and to include the electrons' spin. The model of the power absorption allows for adding electrons to the dot. This involves however increasing the basis to obtain the same precision as for two electrons and program size grows rapidly with electron number. If there were more powerful computers ... The magnetization of the system can be calculated, from knowledge of the energy spectrum of interacting electrons. A repulsive Coulomb potential can be added, describing an impurity in the middle of the dot, to investigate its effect on the absorption spectrum. Such quantum dots have been realized experimentally. Finally, interesting phenomena could occur by calculating the absorption for a confinement potential with an elliptic and a square symmetric confinement term.

Chapter 9

Acknowledgements

The theoretical work presented in this thesis was carried out at the University of Iceland under the supervision of Prof. Viðar Guðmundsson to whom I am indepted for giving me insight into this field of physics. He is a very good supervisor and I thank him for his invaluable support and patience. I thank Prof. Andrei Manolescu for giving a good perspective on many-particle physics and mesoscopic physics in general. I also want to mention Docent Ari Ólafsson who initially encouraged me to pursue the M. Sc. studies at the University of Iceland.

As a part of my M. Sc. studies, courses were taken at the Ecole Normale Supérieure, Rue d'Ulm, Paris, in the program "DEA de Physique Quantique" during the fall semester 1997. I thank Prof. Gerald Bastard and Prof. Jean Dalibard for giving me the opportunity to study there.

The work involved very long running time of programs. I thank in particular Prof. Þórður Jónsson for numerous CPU hours on his Linux machine.

The studies were supported by the University of Iceland Research Fund, the Icelandic Natural Science Foundation and the NorFA Network on Mesoscopic Physics.

I thank my parents for their support throughout my studies.

Appendix A

Matrix elements

A.1 The matrix element $\langle \Phi_j | V_\phi | \Phi_i \rangle$

We wish to evaluate the matrix element of the deviation confinement

$$\langle \Phi_j | V_\phi | \Phi_i \rangle = \int_{\mathbf{R}^2} d\mathbf{r} \Phi_j^*(\mathbf{r}) V_\phi(\mathbf{r}) \Phi_i(\mathbf{r})$$

We write the basis functions (3.3) as

$$\Phi(\mathbf{r}) = \chi(r) e^{-iM\phi}, \tag{A.1}$$

where $r = |\mathbf{r}|$. By writing $i := (M, n_r)$ and $j := (N, m_r)$, the matrix element becomes

$$\langle \Phi_j | V_\phi | \Phi_i \rangle = \int_0^{2\pi} d\phi \int_0^{+\infty} dr r \chi_j(r) e^{iN\phi} V_\phi(\mathbf{r}) \chi_i(r) e^{-iM\phi}. \tag{A.2}$$

The deviation confinement is

$$V_\phi(\mathbf{r}) = \frac{1}{2} m^* \omega_0^2 r^2 \sum_{p=1}^{p^{max}} \alpha_p \cos(2p\phi), \tag{A.3}$$

such that integration over the angle, with the definition $\Delta M := M - N$, gives

$$\sum_{p=1}^{p^{max}} \alpha_p \int_0^{2\pi} d\phi e^{-i\Delta M\phi} \cos(2p\phi) = \sum_{p=1}^{p^{max}} \alpha_p \pi [\delta_{\Delta M, 2p} + \delta_{\Delta M, -2p}]. \tag{A.4}$$

We have thus obtained the selection rule

$$\Delta M = \pm 2p.$$

In view of this selection rule, one can explain lifting of degeneracy of energy levels when the deviation confinement is added to the circular parabolic confinement, if the deviation is small enough. Degenerate states, for which $\Delta M = \pm 2p$, are coupled and the corresponding degeneracy is lifted, as can be explained with perturbation theory. This is discussed in sections 3.2.1 and 3.2.2 for elliptic and square symmetric confinements. This yields

$$\langle\Phi_j|V_\phi|\Phi_i\rangle = \frac{1}{2}m^*\omega_0^2\Big(\frac{n_r!}{(|M|+n_r)!}\Big)^{1/2}\Big(\frac{m_r!}{(|N|+m_r)!}\Big)^{1/2}\sum_{p=1}^{p^{max}}\alpha_p[\delta_{\Delta M,2p}+\delta_{\Delta M,-2p}]$$
$$\times\int_0^{+\infty}dr r\Big(\frac{r^2}{2a^2}\Big)^{\frac{|N|+|M|}{2}+1}e^{-r^2/2a^2}L_{m_r}^{|N|}\Big(\frac{r^2}{2a^2}\Big)L_{n_r}^{|M|}\Big(\frac{r^2}{2a^2}\Big).$$

Change of variables,

$$x=\frac{r^2}{2a^2},\qquad dx=\frac{rdr}{a^2},$$

yields

$$\langle\Phi_j|V_\phi|\Phi_i\rangle = \frac{1}{2}m^*\omega_0^2a^2\Big(\frac{n_r!}{(|M|+n_r)!}\Big)^{1/2}\Big(\frac{m_r!}{(|N|+m_r)!}\Big)^{1/2}$$
$$\times\sum_{p=1}^{p^{max}}\alpha_p[\delta_{\Delta M,2p}+\delta_{\Delta M,-2p}]I_{n_r},$$

where

$$I_{n_r}:=\int_0^{+\infty}dx x^{\frac{|N|+|M|}{2}+1}e^{-x}L_{m_r}^{|N|}(x)L_{n_r}^{|M|}(x).$$

We have the relation (8.975.1 in [26])

$$\sum_{n_r=0}^{+\infty}L_{n_r}^{|M|}(x)t^{n_r}=\frac{e^{-\frac{xt}{1-t}}}{(1-t)^{|M|+1}},\qquad |t|<1,$$

which can be used to evaluate I_{n_r}. This gives

$$\begin{aligned}\sum_{n_r=0}^{+\infty}I_{n_r}t^{n_r}&=\sum_{n_r=0}^{+\infty}t^{n_r}\int_0^{+\infty}x^{\frac{|N|+|M|}{2}+1}e^{-x}L_{m_r}^{|N|}(x)L_{n_r}^{|M|}(x)\,dx\\&=\frac{1}{(1-t)^{|M|+1}}\int_0^{+\infty}x^{\frac{|N|+|M|}{2}+1}e^{-\frac{x}{1-t}}L_{m_r}^{|N|}(x)\,dx\end{aligned}\tag{A.5}$$

$$\begin{aligned}&=(1-t)^{\frac{|N|-|M|}{2}+1}\frac{\Gamma\Big(\frac{|N|+|M|}{2}+2\Big)\Gamma\big(|N|+m_r+1\big)}{m_r!\Gamma\big(|N|+1\big)}\\&\quad\times F\big(-m_r;\tfrac{|N|+|M|}{2}+2;|N|+1;1-t\big)\end{aligned}\tag{A.6}$$

The last relation is given in [26]. The function F is the hypergeometric series (see e.g. [26]) which is in this case a polynomial of order m_r in $(1-t)$. The right hand side of equation (A.6) is therefore a polynomial of order

$$m_r + \frac{|N| - |M|}{2} + 1$$

in $(1-t)$, which can be re-expressed as a polynomial of the same order in t. This yields the selection rule

$$n_r \leq m_r + \frac{|N| - |M|}{2} + 1 \tag{A.7}$$

Since, physically, $n_r \geq 0$, we require that

$$\frac{|N| - |M|}{2} + 1 \geq 0$$

which is acquired if $|N| \geq |M|$ (a stronger condition than necessary). I_{n_r} is however independent of this choice (the interchange $(M, n_r) \leftrightarrow (N, m_r)$ yields the same integral). To evaluate the integral over r for $|M| > |N|$, we simply interchange (M, n_r) and (N, m_r). By writing expression (A.6) as a polynomial in t, we obtain

$$\sum_{n_r=0}^{+\infty} I_{n_r} t^{n_r} = \sum_{n_r=0}^{m_r+l} \sum_{k=0}^{m_r} a_k \binom{k+l}{n_r} (-1)^{n_r} t^{n_r} \tag{A.8}$$

where

$$l = \frac{|N| - |M|}{2} + 1$$

$$a_k = (-1)^k \frac{\left(\frac{|N|+|M|}{2} + 1 + k\right)!}{\left(m_r - k\right)! k!} \frac{\left(|N| + m_r\right)!}{\left(|N| + k\right)!}$$

Comparison of the coefficients in (A.8) then gives that

$$I_{n_r} = \sum_{k=0}^{m_r} a_k \binom{k+l}{n_r} (-1)^{n_r} \tag{A.9}$$

Within some algebraic steps, we have the expression for the matrix element [1]

$$\begin{aligned} \langle \Phi_j | V_\phi | \Phi_i \rangle = {} & \frac{1}{2} m^* \omega_0^2 a^2 \left(\frac{m_r! (|N| + m_r)!}{n_r! (|M| + n_r)!} \right)^{\frac{1}{2}} \sum_{p=1}^{p^{max}} \alpha_p [\delta_{\Delta M, 2p} + \delta_{\Delta M, -2p}] \\ & \times \sum_{k=0}^{m_r} (-1)^{k+n_r} \frac{\left(\frac{|N|+|M|}{2} + k + 1\right)!}{k! \left(m_r - k\right)! \left(|N| + k\right)!} \frac{\left(\frac{|N|-|M|}{2} + k + 1\right)!}{\left(\frac{|N|-|M|}{2} + k + 1 - n_r\right)!} \end{aligned} \tag{A.10}$$

The condition, $|N| \geq |M|$, assures that the quantity on the right side of (A.10) will always be convergent.

[1] Remember however that $\frac{1}{(-n)!} = 0, \quad n = 1, 2, ...$

A.2 The matrix element $\langle\Phi_k|V_H|\Phi_l\rangle$

The Hartree matrix element is given by

$$\langle k|V_H|l\rangle = \int_{\mathbf{R}^2} d\mathbf{r}\Phi_k^*(\mathbf{r})V_H(\mathbf{r})\Phi_l(\mathbf{r}) \tag{A.11}$$

$$= \frac{e^2}{4\pi\epsilon_r\epsilon_0}\int_{\mathbf{R}^2} d\mathbf{r}\Phi_k^*(\mathbf{r})\Big[\int_{\mathbf{R}^2} d\mathbf{r}'\frac{n_s(\mathbf{r}')}{|\mathbf{r}-\mathbf{r}'|}\Big]\Phi_l(\mathbf{r}). \tag{A.12}$$

$1/|\mathbf{r}-\mathbf{r}'|$ can be rewritten [27] as

$$\frac{1}{|\mathbf{r}-\mathbf{r}'|} = \sum_{m=-\infty}^{+\infty} e^{im(\phi-\phi')}\int_0^{+\infty} dkJ_m(kr)J_m(kr') \tag{A.13}$$

where J_m is a Bessel-function of order m and $r = |\mathbf{r}|$. The matrix element then becomes

$$\langle k|V_H|l\rangle = \frac{e^2}{4\pi\epsilon_r\epsilon_0}\int_{\mathbf{R}^2} d\mathbf{r}\Phi_k^*(\mathbf{r})\Big[\int_{\mathbf{R}^2} d\mathbf{r}'\sum_{m=-\infty}^{+\infty} e^{im(\phi-\phi')}\int_0^{+\infty} dkJ_m(kr)J_m(kr')n_s(\mathbf{r}')\Big]\Phi_l(\mathbf{r}). \tag{A.14}$$

We then write the basis functions as in section A.1

$$\Phi(\mathbf{r}) = \chi(r)e^{-iM\phi}. \tag{A.15}$$

The integration over ϕ gives

$$\int_0^{2\pi} d\phi e^{i(m+K-L)\phi} = 2\pi\delta_{m,L-K}. \tag{A.16}$$

For given L and K, only one term in the sum over m is non-zero, namely m=L-K. In order to perform the integration over ϕ', we rewrite the electron density in terms of the basis functions;

$$n_s(\mathbf{r}') = \sum_\alpha f(\varepsilon_\alpha)|\Psi_\alpha(\mathbf{r}')|^2 \tag{A.17}$$

$$= \sum_\alpha f(\varepsilon_\alpha)\sum_{p,q} c_{\alpha p}^* c_{\alpha q}\Phi_p^*(\mathbf{r}')\Phi_q(\mathbf{r}') \tag{A.18}$$

$$= \sum_\alpha f(\varepsilon_\alpha)\sum_{p,q} c_{\alpha p} c_{\alpha q}\Phi_p^*(\mathbf{r}')\Phi_q(\mathbf{r}') \tag{A.19}$$

$$=: \sum_\alpha f_\alpha\sum_{p,q} c_{\alpha p} c_{\alpha q}\chi_p(r')e^{iM\phi'}\chi_q(r')e^{-iN\phi'}. \tag{A.20}$$

We have dropped the asterisk on $c_{\alpha p}$ and $\chi_p(r)$ since they are real quantities. The definitions

$$f_\alpha := f(\varepsilon_\alpha) \tag{A.21}$$

$$p := (M, n_r) \tag{A.22}$$

$$q := (N, m_r) \tag{A.23}$$

have been used in order to compactify the notation. Integration over ϕ' is then readily performed

$$\int_0^{2\pi} d\phi' e^{i(M-N-(L-K))\phi'} = 2\pi\delta_{M-N,L-K}. \tag{A.24}$$

This gives

$$\langle k|V_H|l\rangle = (2\pi)^2 \frac{e^2}{4\pi\epsilon_r\epsilon_0} \sum_\alpha f_\alpha \sum_{p,q} c_{\alpha p} c_{\alpha q} \int_0^{+\infty} dk \Big[\int_0^{+\infty} dr r \chi_k(r) J_{L-K}(kr) \chi_l(r) \Big] \tag{A.25}$$

$$\times \Big[\int_0^{+\infty} dr' r' \chi_p(r') J_{M-N}(kr') \chi_q(r') \Big] \delta_{M-N,L-K}. \tag{A.26}$$

Put

$$\chi_k(r) := \beta_k \Big(\frac{r}{a}\Big)^{|K|} \exp(-r^2/4a^2) L_{k_r}^{|K|}\Big(\frac{r^2}{2a^2}\Big), \tag{A.27}$$

with

$$\beta_k := \frac{1}{2^{\frac{|K|+1}{2}} a} \Big(\frac{k_r!}{\pi(|K|+k_r)!}\Big)^{1/2} \tag{A.28}$$

and similarly for the other wavefunctions. This gives

$$\langle k|V_H|l\rangle = (2\pi)^2 \frac{e^2}{4\pi\epsilon_r\epsilon_0} \beta_k\beta_l \sum_\alpha f_\alpha \sum_{p,q} c_{\alpha p} c_{\alpha q} \beta_p\beta_q \delta_{M-N,L-K} \tag{A.29}$$

$$\times \int_0^{+\infty} dk \Big[\int_0^{+\infty} dr r \Big(\frac{r}{a}\Big)^{|K|+|L|} \exp(-r^2/2a^2) L_{k_r}^{|K|}\Big(\frac{r^2}{2a^2}\Big) L_{l_r}^{|L|}\Big(\frac{r^2}{2a^2}\Big) J_{L-K}(kr) \Big] \tag{A.30}$$

$$\times \Big[\int_0^{+\infty} dr' r' \Big(\frac{r'}{a}\Big)^{|M|+|N|} \exp(-r'^2/2a^2) L_{n_r}^{|M|}\Big(\frac{r'^2}{2a^2}\Big) L_{m_r}^{|N|}\Big(\frac{r'^2}{2a^2}\Big) J_{M-N}(kr') \Big]. \tag{A.31}$$

The Batemann manuscripts [28] give the solution to this type of integrals but only with the restriction that K and L (M and N) need to be of opposite sign. To obtain a general answer, we rewrite the Laguerre functions as polynomials

$$L_{n_r}^{|M|}\Big(\frac{r^2}{2a^2}\Big) = \sum_{\nu=0}^{n_r} \frac{(-1)^\nu}{2^\nu \nu!} \binom{n_r + |M|}{n_r - \nu} \Big(\frac{r}{a}\Big)^{2\nu}. \tag{A.32}$$

The matrix elements then transform into

$$\begin{aligned}\langle k|V_H|l\rangle = (2\pi)^2 \frac{e^2}{4\pi\epsilon_r\epsilon_0}\beta_k\beta_l \sum_\alpha f_\alpha \sum_{p,q} c_{\alpha p}c_{\alpha q}\beta_p\beta_q \sum_{\kappa=0}^{k_r}\sum_{\lambda=0}^{l_r}\sum_{\nu=0}^{n_r}\sum_{\mu=0}^{m_r} \frac{(-1)^{\kappa+\lambda+\nu+\mu}}{\kappa!\lambda!\nu!\mu!} \\ \times \binom{k_r+|K|}{k_r-\kappa}\binom{l_r+|L|}{l_r-\lambda}\binom{n_r+|M|}{n_r-\nu}\binom{m_r+|N|}{m_r-\mu} \\ \times \int_0^{+\infty} dk \frac{1}{2^{\kappa+\lambda}}\Big[\int_0^{+\infty} drr\Big(\frac{r}{a}\Big)^{|K|+|L|+2(\kappa+\lambda)} \exp(-r^2/2a^2)J_{L-K}(kr)\Big] \\ \times \frac{1}{2^{\nu+\mu}}\Big[\int_0^{+\infty} dr'r'\Big(\frac{r'}{a}\Big)^{|M|+|N|+2(\nu+\mu)} \exp(-r'^2/2a^2)J_{M-N}(kr')\Big].\end{aligned}$$

We have that [26]

$$\begin{aligned}\int_0^{+\infty} drr\Big(\frac{r}{a}\Big)^{|K|+|L|+2(\kappa+\lambda)} \exp(-r^2/2a^2)J_{L-K}(kr) \\ = 2^{\frac{|K|+|L|+K-L}{2}+\kappa+\lambda}(ka)^{L-K}a^2\frac{\Gamma\big(\frac{L-K+|K|+|L|}{2}+\kappa+\lambda+1\big)}{\Gamma(L-K+1)} \\ \times {}_1F_1\Big(\frac{L-K+|K|+|L|}{2}+\kappa+\lambda+1; L-K+1; -\frac{k^2a^2}{2}\Big),\end{aligned}$$

where ${}_1F_1$ is a confluent hypergeometric function, defined on p. 1085 in [26]. The integral over r' is of the same kind;

$$\begin{aligned}\int_0^{+\infty} dr'r'\Big(\frac{r'}{a}\Big)^{|M|+|N|+2(\nu+\mu)} \exp(-r'^2/2a^2)J_{M-N}(kr') \\ = 2^{\frac{|M|+|N|+N-M}{2}+\nu+\mu}(ka)^{M-N}a^2\frac{\Gamma\big(\frac{M-N+|M|+|N|}{2}+\nu+\mu+1\big)}{\Gamma(M-N+1)} \\ \times {}_1F_1\Big(\frac{M-N+|M|+|N|}{2}+\nu+\mu+1; M-N+1; -\frac{k^2a^2}{2}\Big).\end{aligned}$$

With the redefinition

$$\gamma_k := (2\pi)^{1/2}2^{\frac{|K|}{2}}a\beta_k = \Big(\frac{k_r!}{(|K|+k_r)!}\Big)^{1/2}$$

and with aid of the selection rule $L-K=M-N$, one obtains

$$\begin{aligned}\langle k|V_H|l\rangle = \frac{e^2}{4\pi\epsilon_r\epsilon_0}\gamma_k\gamma_l\sum_\alpha f_\alpha\sum_{p,q}c_{\alpha p}c_{\alpha q}\gamma_p\gamma_q\sum_{\kappa=0}^{k_r}\sum_{\lambda=0}^{l_r}\sum_{\nu=0}^{n_r}\sum_{\mu=0}^{m_r}\frac{(-1)^{\kappa+\lambda+\nu+\mu}}{\kappa!\lambda!\nu!\mu!}\\ \times\binom{k_r+|K|}{k_r-\kappa}\binom{l_r+|L|}{l_r-\lambda}\binom{n_r+|M|}{n_r-\nu}\binom{m_r+|N|}{m_r-\mu}\\ \times\frac{\Gamma\left(\frac{L-K+|K|+|L|}{2}+\kappa+\lambda+1\right)}{\Gamma(L-K+1)}\frac{\Gamma\left(\frac{M-N+|M|+|N|}{2}+\nu+\mu+1\right)}{\Gamma(M-N+1)}\\ \times\int_0^{+\infty}dk\left(\frac{k^2a^2}{2}\right)^{L-K}{}_1F_1\left(\frac{L-K+|K|+|L|}{2}+\kappa+\lambda+1;L-K+1;-\frac{k^2a^2}{2}\right)\\ \times{}_1F_1\left(\frac{M-N+|M|+|N|}{2}+\nu+\mu+1;M-N+1;-\frac{k^2a^2}{2}\right).\end{aligned}$$

This last integral can be evaluated analytically, giving a hypergeometric function of several variables (definition p. 1084 in [26]). This is achieved by writing ${}_1F_1$ in terms of a Whittaker function, $M_{\lambda,\mu}$, via the relation

$$M_{\lambda,\mu}(x)=x^{\mu+\frac{1}{2}}e^{-x/2}{}_1F_1(\mu-\lambda+\frac{1}{2},2\mu+1;x)$$

and we also have

$${}_1F_1(\alpha,\gamma;x)=e^x{}_1F_1(\gamma-\alpha,\gamma;-x).$$

The integral can then be evaluated from 7.622.3 in [26], giving the hypergeometric function F_2 of several variables. This function is however not very practical in use. Therefore, it has been chosen to evaluate the integral over k numerically.

Bibliography

[1] P. A. Maksym and T. Chakraborty, Phys. Rev. Lett. **65**, 108 (1990).

[2] S. K. Yip, Phys. Rev. B **43**, 1707 (1991).

[3] D. Pfannkuche, Habilitation Thesis, University of Karlsruhe, Germany, 1998.

[4] T. Ando, A. B. Fowler, and F. Stern, Rev. of Mod. Phys. **54**, 437 (1982).

[5] M. Hochgräfe, Diploma thesis, University of Hamburg, Germany, 1998.

[6] T. Kurth, Ph.D. thesis, University of Hamburg, Germany, 1998.

[7] V. Gudmundsson *et al.*, Phys. Rev. B **51**, 17744 (1995).

[8] T. Demel, D. Heitmann, P. Grambow, and K. Ploog, Phys. Rev. Lett. **64**, 788 (1990).

[9] C. Cohen-Tannoudji, B. Diu, and F. Laloë, *Quantum Mechanics* (John Wiley & Sons, New-York, 1977), Vol. I.

[10] W. Kohn, Phys. Rev. **123**, 1242 (1961).

[11] L. Brey, N. F. Johnson, and B. I. Halperin, Phys. Rev. B **40**, 10647 (1989).

[12] P. Bakshi, D. A. Broido, and K. Kempa, Phys. Rev. B **42**, 7416 (1990).

[13] Q. P. Li *et al.*, Phys. Rev. B **43**, 5151 (1991).

[14] V. Fock, Z. Phys. **47**, 446 (1928).

[15] C. G. Darwin, Proc. Camb. Phil. Soc. **27**, 86 (1930).

[16] E. K. U. Gross, E. Runge, and O. Heinonen, *Many-Particle Theory* (Adam Hilger, Bristol, 1991).

[17] V. Gudmundsson and A. S. Loftsdóttir, Phys. Rev. B **50**, 17433 (1994).

[18] C. Steinebach, Ph.D. thesis, University of Hamburg, Germany, 1998.

[19] T. Jonsson and J. Yngvason, *Waves and distributions* (World Scientific, Singapore, 1995).

[20] T. Ezaki, N. Mori, and C. Hamaguchi, Phys. Rev. B **56**, 6428 (1997).

[21] A. V. Madhav and T. Chakraborty, Phys. Rev. B **49**, 8163 (1994).

[22] C. Dahl, Ph.D. thesis, Ludwig-Maximilians-Universität, München, Germany, 1992.

[23] E. Vasiliadou, Ph.D. thesis, University of Hamburg, Germany, 1995.

[24] I. B. Bernstein, Phys. Rev. **109**, 10 (1958).

[25] D. Pfannkuche and R. R. Gerhardts, Phys. Rev. B **44**, 13132 (1991).

[26] I. S. Gradshteyn and I. M. Ryzhik, in *Table of Integrals, Series, and Products*, edited by A. Jeffrey (Academic Press, San Diego, 1994).

[27] J. D. Jackson, *Classical Electrodynamics* (John Wiley & Sons, New York, 1975).

[28] *Tables of Integral Transforms*, edited by A. Erdélyi (McGraw-Hill Book Company, New York, 1954), Vol. II.